ORIGINAL ARTICLE



Modeling of sustained spontaneous network oscillations of a sexually dimorphic brainstem nucleus: the role of potassium equilibrium potential

Daniel Hartman¹ Dávid Lehotzky¹ Lulian Ilies¹ Mariana Levi² Günther K. H. Zupanc¹

Received: 4 March 2021 / Revised: 15 April 2021 / Accepted: 29 April 2021 / Published online: 25 May 2021 © The Author(s), under exclusive licence to Springer Science+Business Media, LLC, part of Springer Nature 2021

Abstract

Intrinsic oscillators in the central nervous system play a preeminent role in the neural control of rhythmic behaviors, yet little is known about how the ionic milieu regulates their output patterns. A powerful system to address this question is the pacemaker nucleus of the weakly electric fish *Apteronotus leptorhynchus*. A neural network comprised of an average of 87 pacemaker cells and 20 relay cells produces tonic oscillations, with higher frequencies in males compared to females. Previous empirical studies have suggested that this sexual dimorphism develops and is maintained through modulation of buffering of extracellular K^+ by a massive meshwork of astrocytes enveloping the pacemaker and relay cells. Here, we constructed a model of this neural network that can generate sustained spontaneous oscillations. Sensitivity analysis revealed the potassium equilibrium potential, E_K (as a proxy of extracellular K^+ concentration), and corresponding somatic channel conductances as critical determinants of oscillation frequency and amplitude. In models of both the pacemaker nucleus network and isolated pacemaker and relay cells, the frequency increased almost linearly with E_K , whereas the amplitude decreased nonlinearly with increasing E_K . Our simulations predict that this frequency increase is largely caused by a shift in the minimum K^+ conductance over one oscillation period. This minimum is close to zero at more negative E_K , converging to the corresponding maximum at less negative E_K . This brings the resting membrane potential closer to the threshold potential at which voltage-gated Na^+ channels become active, increasing the excitability, and thus the frequency, of pacemaker and relay cells.

Keywords Astrocytes · Central pattern generator · Computational modeling · Potassium equilibrium · Sexual dimorphism · Sustained spontaneous oscillations

1 Introduction

Sex differences in behavior are one of the best-characterized phenomena in ethology (for review see Kelley, 1988). However, much less is known about the morphological and physiological features that control such sexual dimorphism in the

Communicated by Action Editor: Catherine E Carr.

Daniel Hartman and Dávid Lehotzky contributed equally to this work

- Günther K. H. Zupanc g.zupanc@northeastern.edu
- ¹ Laboratory of Neurobiology, Department of Biology, Northeastern University, Boston, MA 02115, USA
- Research Computing, Northeastern University, Boston, MA 02115, USA

central nervous system (CNS). An organism in which both aspects can be readily studied is the brown ghost knifefish (Apteronotus leptorhynchus). This gymnotiform species possesses an electric organ formed by electrocytes — enlarged axonal terminals of modified spinal motoneurons known as electromotoneurons (Bennett, 1971; de Oliveira-Castro, 1955; Waxman et al., 1972). The synchronized discharge of the electrocytes produces the electric organ discharge (EOD). The frequency of the EOD (f_{EOD}) is highly constant in a given fish but varies among individuals within the 650-1000 Hz range, with males typically generating discharges at higher frequencies than females and very little overlap between the two sexes (Meyer et al., 1987; Zupanc et al., 2014). Behavioral experiments have suggested that this sexual dimorphism in $f_{\rm EOD}$ aids sex recognition in A. leptorhynchus (Engler & Zupanc, 2001). The development and maintenance of this sex-specific difference is under control of steroid hormones, as indicated by a robust



gradual decrease in $f_{\rm EOD}$ following chronic administration of β -estradiol (Meyer et al., 1987; Schaefer & Zakon, 1996; Zupanc et al., 2014).

The brain structure that controls f_{EOD} is the pacemaker nucleus (Pn) (for review see Dye & Meyer, 1986). Neural oscillations of this brainstem nucleus drive the EOD, via a descending volley of spikes, in a one-to-one fashion, i.e., $f_{\rm EOD}$ equals the frequency of the Pn, $f_{\rm Pn}$. Several types of neurons have been identified in the Pn: two subpopulations of small interneurons, with overlapping size distributions but differing in morphology (Sîrbulescu et al., 2014; Smith et al., 2000; Turner & Moroz, 1995); and two morphologically distinct populations of large neurons, with somatic diameters between 25-40 µm in the former and 50-70 µm in the latter, referred to as pacemaker and relay cells, respectively (Dye & Heiligenberg, 1987; Elekes & Szabo, 1985; Sîrbulescu et al., 2014). The two types of large neurons have been shown to be critically involved in the generation of Pn oscillations (for review see Dye & Meyer, 1986). Their numbers are remarkably similar across adult fish (mean ± standard error (SE) of 87 ± 4 pacemaker cells and 20 ± 1 relay cells) and independent of the individual's sex (Sîrbulescu et al., 2014). Pacemaker cells are extensively coupled to each other as well as to relay cells through electrotonic synapses. While the somata of both cell types are confined to the Pn, the axons of relay cells project to the spinal cord to form electrotonic junctions with the electromotoneurons. By contrast, the function and connectivity patterns of the small interneurons are currently unknown, and they outnumber pacemaker and relay cells roughly 50-fold, making accurate modeling challenging. Accordingly, they were not considered further in the present study.

A remarkable feature of the Pn is the large number of astrocytes it contains, estimated at approximately 40,000 in the average adult fish (Sîrbulescu et al., 2014). Thus, they outnumber pacemaker and relay cells almost 400-fold, and all identified Pn neurons (total of approximately 5,400) 7-fold. For comparison, glia-to-neuron ratios were estimated at 0.5–2 in mammalian brains (Hilgetag & Barbas, 2009; von Bartheld et al., 2016), congruent with the 2:1 ratio of \$100-expressing astrocytic cells to Hu C/D-expressing neurons found in the spinal cord of *A. leptorhynchus* (Sîrbulescu et al., 2017). Thus, the large relative number of astrocytes versus neurons appears to be specific to the Pn, and not to the CNS of this organism in general. The tremendous abundance of astroglia in the Pn is paralleled by an extremely high rate of gliogenesis (Sîrbulescu et al., 2014).

What might be the function of the enormous number of astrocytes in the Pn? It has been hypothesized that operation of the ATP-fueled Na^+/K^+ pump is sufficient to remove K^+ ions from the extracellular space and cycle them back

to neurons during low-frequency firing in other CNS subsystems. However, it is thought that buffering and redistribution of extracellular K⁺ during high-frequency firing are instead primarily achieved through the action of the surrounding astrocytes (Lux et al., 1986; Somjen, 2004). Given the lifelong continuous firing of pacemaker and relay cells at extremely high frequencies (0.6–1 kHz), and the resulting release of massive amounts of K⁺ from these cells into the extracellular space, it is plausible that one of the chief functions of the Pn astrocytic meshwork is to buffer the continuous increase in the extracellular concentration of potassium, [K⁺], by means of specific K⁺ channels. Following uptake of extracellular K⁺, the abundant coupling of astrocytes via gap junctions, as indicated by the intense connexin-43 immunoreactivity associated with these cells (Zupanc et al., 2014), might serve as a mechanism to aid redistribution of K⁺ from sites of excessive levels to sites of lower K⁺ concentrations within the Pn.

Notably, the morphology and expression patterns of Pn astrocytes exhibit pronounced sexual dimorphisms (Zupanc et al., 2014). Both the surface area of pacemaker and relay cells covered by glial fibrillary acidic protein (GFAP)-expressing astrocytes, as well as the overall intensity of GFAP expression within the Pn, are markedly higher in females than in males. In addition, gap-junction coupling within the astrocytic syncytium is also significantly stronger in females, as suggested by sex-dependent differences in expression of the gap-junction protein connexin-43. Similar to the development of the sexual dimorphism of $f_{\rm EOD}$, the morphology and expression pattern of the astrocytic syncytium are under control of steroid hormones, as suggested by chronic implantation experiments (Zupanc et al., 2014).

Our working hypothesis is that modulation of extracellular K⁺ buffering by the astrocytic syncytium associated with pacemaker and relay cells is a key mechanism for regulating $f_{\rm Pn}$, and thus for the development and the maintenance of the sexual dimorphism in $f_{\rm EOD}$ (Zupanc, 2017, 2020; Zupanc et al., 2014, 2019). In the present study, we addressed this hypothesis from a modeling point of view, which provided a theoretical foundation to explore the relationship between the potassium equilibrium potential, E_{K} , and f_{Pn} . We first constructed a computational model of the Pn neural network that can generate sustained spontaneous oscillations in a similar frequency range as its biological counterpart. Then, we used this model to examine the effect of variations in E_{K} , assumed to reflect changes in $[K^+]_0$, on the frequency and amplitude of oscillations produced by the network. Insights from this work could help design in vivo or in vitro experiments that more accurately probe the morphological and physiological features controlling sexual dimorphisms in a specific CNS system.



2 Methods

2.1 Modeling of pacemaker and relay cells

Pacemaker and relay cells were modeled using the NEURON Simulation Environment (version 7.7) (Hines & Carnevale, 1997) with Python (version 3.7) as the interpreter (Hines et al., 2009). Each cell consisted of two cylindrical compartments (somatic and axonal) subdivided into 1-μm long segments expressing Hodgkin-Huxley ion channels, with parameter specifications (segment sizes and electrical properties, channel conductances, and equilibrium potentials) derived from morphological and biophysical data (Dye, 1991; Dye & Heiligenberg, 1987; Elekes & Szabo, 1985; Juranek & Metzner, 1998; Moortgat et al., 2000a; Shifman et al., 2020; Sîrbulescu et al., 2014) (Table 1). Ion channel kinetics were scaled to 27 °C, the mean water temperature at which *A. leptorhynchus* is kept in our laboratory.

2.2 Modeling of pacemaker nucleus network

The Pn was modeled as a network consisting of 87 pacemaker cells and 20 relay cells, reflecting the average counts of these two neuronal cell types in *A. lepto-rhynchus* (Sîrbulescu et al., 2014). Consistent with cell morphological data (Dye & Heiligenberg, 1987; Elekes & Szabo, 1985; Moortgat et al., 2000a; Yamamoto et al., 1989; Zupanc et al., 2014) and previous modeling studies (Lucas et al., 2019; Moortgat et al., 2000b; Zupanc et al., 2019), each pacemaker cell made synaptic contact via rectifying gap junctions with exactly 6 other unique pacemaker cells and 7 unique relay cells, randomly selected from the corresponding populations (see Fig. 1a for a typical network; created using Gephi version 0.9.2 (Bastian

et al., 2009)). Since it is currently unknown whether gapjunction coupling strength differs between pacemaker cells making synaptic contact with other pacemaker cells, and pacemaker cells making such contacts with relay cells, we assumed the conductances for these two connection types to be identical. Relay cells did not project to any other Pn network cell, and their axonal endings were left closed.

Rectifying gap junctions were implemented using the model description language NMODL (Hines & Carnevale, 2000) and assumed a mechanism with instantaneous rectification. They were modeled as two NEURON point processes attached to the last axonal segment of the presynaptic cell and the first somatic segment of the postsynaptic cell. Their conductivity was allowed to vary within an operable range of [0.5, 10.0] nS proportionally to the voltage difference between the presynaptic and postsynaptic cell, consistent with their experimentally-determined properties (Giaume et al., 1987; Gutierrez & Marder, 2013; Spray et al., 1981). The underlying point processes were set to monitor the membrane potential, V, of each segment and then deliver the correct amount of current to it based upon the varied conductance (Gutierrez & Marder, 2013).

2.3 Numerical simulation of neural activity patterns

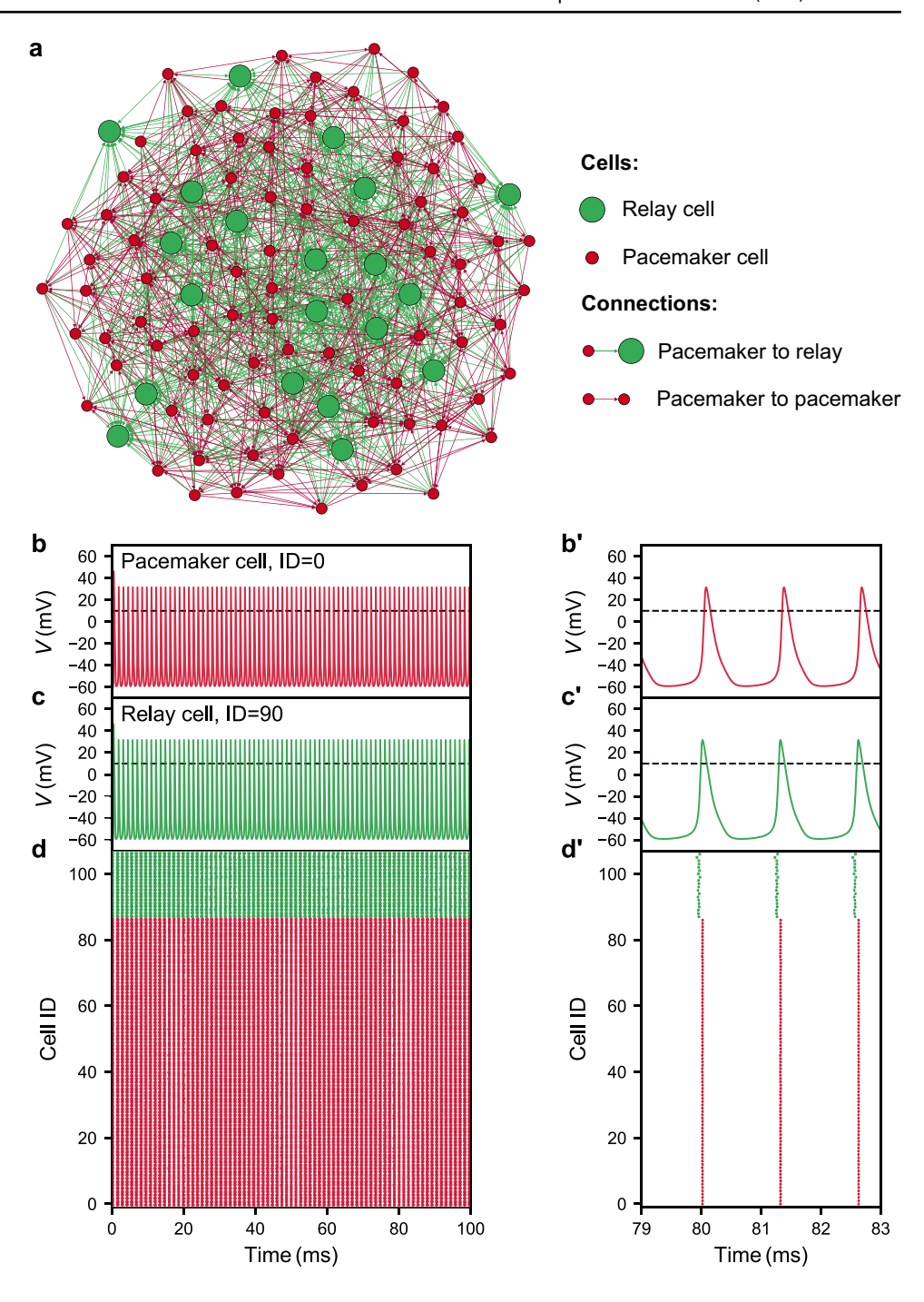
Pn networks, as well as isolated pacemaker and relay cells, were simulated for a total of 100 ms under spontaneous conditions only (i.e., without injecting current), with over 1.5 million independent scenarios conducted during this study. All simulations were initialized from V = -65 mV for all segments in all cells, and numerically integrated using a variable time step via NEURON's adaptive integration feature. Simulations were performed on a MacBook Pro 2019 (8-core Intel Core i9 CPU at 2.3 GHz with 16 GB RAM) and the Discovery cluster of Northeastern University (up to 20

Table 1 Morphological and biophysical parameters of model pacemaker and relay cells

	Notation	Pacemaker Cells		Relay Cells	
Parameter		Soma	Axon	Soma	Axon
Segments	nseg (unitless)	30	45	65	40
Length	$L (\mu m)$	30.0	45.0	65.0	40.0
Diameter	$D (\mu m)$	30.0	8.0	65.0	7.0
Axial resistivity	$R_{\rm a} (\Omega \cdot {\rm cm})$	100.0	100.0	100.0	500.0
Specific membrane capacitance	$C_{\rm m}$ ($\mu F/cm^2$)	1	1	1	1
Maximum specific Na ⁺ channel conductance	$g_{\text{Na}} (\text{S/cm}^2)$	[0, 2.0] or 1.0	0.5	[0, 2.0] or 0.75	0.5
Maximum specific K ⁺ channel conductance	$g_{\rm K}$ (S/cm ²)	[0, 0.2]	0.02	[0, 0.2]	0.05
Specific leak conductance	$g_{\rm L}$ (S/cm ²)	0.0001	0.001	0.0003	0.001
Na ⁺ equilibrium potential	$E_{\mathrm{Na}}(\mathrm{mV})$	[0, 100] or 50	[0, 100] or 50	[0, 100] or 50	[0, 100] or 50
K ⁺ equilibrium potential	$E_{\rm K}$ (mV)	[-150, -50]	[-150, -50]	[-150, -50]	[-150, -50]
Leak equilibrium potential	$E_{\rm L}$ (mV)	-70.0	-70.0	-70.0	-70.0
Ambient temperature	<i>T</i> (°C)	27.0	27.0	27.0	27.0



Fig. 1 a Sample connectivity graph of a model Pn network composed of 87 pacemaker cells (red) and 20 relay cells (green). Each pacemaker cell randomly connects to 6 unique pacemaker cells (red arrows) and 7 unique relay cells (green arrows) through axo-somatic, rectifying gap junctions. b-d, b'-d' Sustained spontaneous oscillations of the simulated Pn. Parameters were set to $E_{\rm K} = -60 \text{ mV}, E_{\rm Na} = 50 \text{ mV},$ somatic $g_K = 0.1 \text{ S/cm}^2$, somatic $g_{\text{Na}} = 1 \text{ S/cm}^2$, and as detailed in Table 1. b, c Membrane potential over time for a sample pacemaker cell (identifier 0 in d, d') and a sample relay cell (identifier 90 in d, d'), respectively. d Spike raster plot of the simulated neural activity of all pacemaker cells (red) and relay cells (green) within the modeled network. Each row corresponds to one cell (identifier shown on the vertical axis). For each cell, dots along the horizontal axis mark the times at which its membrane potential crossed the 10-mV threshold (dashed black horizontal line in b, c, b', c') during action potential generation. b'-d' Close-up view of a 4 ms interval from **b-d**, illustrating the waveform of individual action potentials (b', c'). Note small positive phase shift between pacemaker and relay cells and slight de-synchronization among the latter population (d')



nodes with dual 28-core Intel Xeon Platinum 8276 CPUs at 2.20 GHz and 256 GB RAM each).

To decrease total wall time for experiments involving large numbers of scenarios, simulations were distributed across up to 1,024 CPUs using a batch-style divide and conquer parallelization setup leveraging NEURON's ParallelContext module and OpenMPI (version 4.0.2). Individual simulations were distributed evenly among 128 jobs, each allocating up to 500 CPU cores, which were run 2 to 8 at a time depending on the total number of scenarios in the

batch. Each job maintained a Parallel Workers model, where a delegator process distributed tasks (individual simulations) to different workers (MPI processes). These workers ran in parallel on different cores, and were assigned new tasks as they completed their current ones, thus minimizing idle CPU time and increasing CPU efficiency. For very large batches (over 500,000 scenarios), two such job groups were run in parallel, each allocating 500 CPU cores. Results were aggregated from their respective job directories once all jobs were completed.



2.4 Identification of sustained spontaneous oscillations

Membrane potential traces were collected from the somatic compartment of each modeled cell, adjacently to where it connected to the axonal segment. This location corresponds to the axon hillock in the real cell. Action potentials were defined as time points when V crossed from below to above an activation threshold of 10 mV (Fig. 1b, b', c, c'). Time stamps of action potentials were extracted to one-dimensional arrays (raster plots; Fig. 1d, d') and used to compute interspike intervals, separately for each cell. The firing frequency of an individual cell was calculated as the inverse of the final interspike interval (oscillation period) within the simulated time range if it fired more than once, or 0 otherwise. The corresponding amplitude was calculated as the difference between the maximum and minimum of V during the second half of the simulation if the cell fired more than once, or 0 otherwise.

The frequency of the Pn network was defined as that of the fastest firing (highest frequency) relay cell, if the following conditions were satisfied:

- The fastest firing cells from the pacemaker and relay populations fired more than once during the course of the simulation.
- 2. The fastest firing cell of each population continued firing until the end of the simulation, as determined by the final action potential occurring within the last third of the simulated period of 100 ms.
- The frequency of the fastest pacemaker cell was within ± 50% of that of the fastest relay cell. This tolerance was chosen to account for the spike doubling occurring in relay cells at certain parameter combinations.

Simulations that did not meet these criteria were considered to not exhibit sustained oscillations. They were assigned a small negative value as frequency for numerical analysis purposes (see Sect. 2.7 below).

2.5 Sensitivity analysis of sustained spontaneous oscillations

To acquire a basic understanding of the prevalence of, and conditions for, sustained spontaneous oscillations in the Pn, as well as to identify key parameters and value ranges for subsequent experiments, we performed a systematic assessment of the six-dimensional parameter space consisting of $E_{\rm K}$, the sodium equilibrium potential, $E_{\rm Na}$, and corresponding somatic channel conductances, $g_{\rm K,pacemaker}$, $g_{\rm K,relay}$, $g_{\rm Na,pacemaker}$, and $g_{\rm Na,relay}$, using a full factorial design. Each parameter was varied across its range (Table 1) in 9

equal increments (10 points), for a total of 1 million combinations. Simulation outputs, including occurrence of sustained spontaneous oscillations and corresponding frequency, if defined, were analyzed using generalized linear models with distribution-appropriate (binomial, respectively normal) link functions. Fitted models included quadratic terms to account for any non-linearity, and pairwise interaction terms to identify any sets of parameters that cannot be examined independently of each other in follow-up experiments. Input parameters were normalized to the [-1, 1] range prior to analysis to enable direct comparison of all considered factors and interactions. Statistical significance levels of the resulting fit coefficients were computed via conversion to a t-statistic (equal to the ratio between each estimate and its SE), and adjusted for multiple comparisons using the Bonferroni method, separately for each fit. Factors were sorted by decreasing absolute value of their range-standardized coefficients as a measure of effect size, both globally and within each category of factors (linear, quadratic, and interaction).

2.6 Bifurcation analysis of the Hodgkin-Huxley equations

To test whether Pn sustained spontaneous oscillations are a network property or driven by the firing of individual cells, and, furthermore, to determine whether the Hodgkin-Huxley equations (Hodgkin & Huxley, 1952) can provide a robust approximation for the network behavior, we performed bifurcation analyses of these equations with respect to the critical parameter $E_{\rm K}$. We considered two cases: the soma of an isolated pacemaker cell, and the soma of an isolated relay cell. In both cases, the injected and gap junction currents were set to zero, and the remaining parameters (including $g_{\rm K}$, $g_{\rm Na}$, $E_{\rm Na}$, as well as the leak equilibrium potential, $E_{\rm L}$, and corresponding conductance, $g_{\rm L}$) were fixed in accordance with Table 1.

Bifurcation analyses were carried out using the MATCONT environment (Dhooge et al., 2003) version 6.11 with MATLAB version 9.8 as the interface. The bifurcation continuation was initialized from stable equilibria obtained from simulations run at $E_K = -80$ mV starting from the initial condition [V, n, m, h] = [-30, 0.2, 0.2, 0.2], where n, m, h are the Hodgkin-Huxley gate functions (for detailed formulae and notation of the Hodgkin-Huxley equations, see (Zupanc et al., 2019)). Equilibrium curves and branches growing out from these curves were followed until the branches disappeared or left the $E_K \in [-150, -50]$ mV range of interest. The completeness of bifurcation diagrams within the range of interest was systematically checked via simulations started from $V \in [-150, 100]$ mV and $n, m, h \in [0, 1]$.

In addition, to gain insights into how different ion channels contribute to the generation of action potentials, we simulated the Hodgkin-Huxley equation models at $E_{\rm K}$ values



where V exhibited sustained oscillations. We varied $E_{\rm K}$ for pacemaker cells between [-74.7, -55.3] mV in 300 equal steps, and for relay cells between [-71.0, -52.6] mV in 200 equal steps. In each case, we examined the dynamics of V, $g_{\rm K}$, and $g_{\rm Na}$ during a single sustained-spontaneous-oscillation time-period. We computed the maxima and minima of channel conductances and their phases (time differences normalized to the oscillation period) relative to the peak of V, and we determined their trends within the tested $E_{\rm K}$ ranges.

2.7 Identification of parameter regions associated with sustained oscillations

We implemented in Python a multidimensional bisection method combined with solution patch continuation to determine the boundaries between the occurrence of sustained spontaneous oscillations and the absence of such synchronous neural activity. Compared to a simple grid search, this algorithm reduced runtimes by about two orders of magnitude. Our method is similar to that of Bachrathy and Stépán (2012), and consists of the following three steps:

- 1. Initialization: The *n*-dimensional parameter space of interest is divided into $(m_1 1)(m_2 1) \dots (m_n 1)$ equisized *n*-cubes (as for a simple grid search), where m_i is the number of equidistant nodes along coordinate *i*.
- 2. Bisection iteration: The coarse initial grid is iteratively refined such that all n-cubes whose nodes are not all associated with either sustained spontaneous oscillations $(f_{Pn} > 0)$ or the absence of this behavior $(f_{Pn} < 0)$, henceforth called bracketing cubes, are halved along each dimension. After a fixed count k of iterative refinement steps, the resulting final grid has a resolution of $(m_i 1) / 2^k$ along each coordinate i near the boundaries of the region of interest $(f_{Pn} = 0)$.
- 3. Patch continuation: For each bracketing cube produced at the final iteration, it is checked whether all 2^n of its n-cube neighbors (of the same size) have been evaluated. If not, then $f_{\rm Pn}$ is calculated at the nodes of missing neighbors, and it is determined whether these newly generated n-cubes are bracketing cubes. This procedure is repeated iteratively for all newly added bracketing cubes until all neighbors of such cubes have been assessed.

We applied this approach to the parameter space defined by $E_{\rm K}$, $g_{\rm K,pacemaker}$, and $g_{\rm K,relay}$ (i.e., $n\!=\!3$). The iterative bisection step was initialized with a uniform three-dimensional grid consisting of $9\!\times\!7\!\times\!7$ points spanning $E_{\rm K}\!\in\![-150,-50]$ mV, respectively $g_{\rm K,pacemaker}$ and $g_{\rm K,relay}$ values between 0 and 0.2 S/cm² (limits included). All remaining parameters were fixed to the values listed in Table 1. This initial grid was iteratively refined (halved) as long as the total number

of nodes did not exceed 1 million (here, five times). This generated a final resolution of 0.391 mV for $E_{\rm K}$, respectively 1.04 mS/cm² for $g_{\rm K,pacemaker}$ and $g_{\rm K,relay}$. Subsequently, the detected solution surfaces were followed until all surfaces either became enclosed or reached the boundary of the considered parameter space.

Code files implementing the NEURON model and the batch simulation and optimization algorithms described above (Sects. 2.1–2.4 and 2.7) are available in a public GitHub repository at the following link: https://github.com/LaboratoryOfNeurobiology/modeling-sustained-spontaneous-brainstem-oscillations.git

3 Results

3.1 Sensitivity analysis reveals widespread occurrence of sustained spontaneous oscillations in the network model

Systematic examination of 1 million parameter combinations uniformly distributed within the six-dimensional space defined by $E_{\rm K}$, $E_{\rm Na}$, and the corresponding channel conductances revealed widespread occurrence of sustained spontaneous oscillations (Fig. 2). Nearly 5% of the performed simulations resulted in such oscillations, encompassing $E_{\rm K}$ values ranging from –150 to –61 mV, $E_{\rm Na}$ values between 11 and 100 mV, and all evaluated pacemaker and relay cell channel conductance values — including 0 S/cm² (i.e., without active conductances). In particular, 0.2% (113) of the parameter sets yielding sustained oscillations featured passive relay cells, 0.1% (69) had passive pacemaker cells, and 0.4% (211) were missing active K+ channels on the somata of either cell type (Fig. 2b).

Corresponding Pn frequencies ranged from as low as 12 Hz to as high as 1366 Hz and followed a pronouncedly multi-modal distribution, including groups centered at 110 Hz (11% of solutions), 230 Hz (47%), 420 Hz (3%), 690 Hz (19%), 780 Hz (18%), and 1150 Hz (2%) (Fig. 3a). Solutions with $f_{\rm Pn}$ between 650–1000 Hz (i.e., within empirically observed ranges) were characterized by $E_{\rm K}$ close to –60 mV, right-skewed distributions for $g_{\rm K,pacemaker}$ and $g_{\rm K,relay}$ (centered near 0.15 S/cm²), $E_{\rm Na} \ge 20$ mV (centered near 50 mV), and $g_{\rm Na,pacemaker}$ and $g_{\rm Na,relay} > 0.2$ S/cm² (centered near 1.3, respectively 0.9 S/cm²) (Fig. 3b).

Statistical analysis of sustained oscillation incidence using a logistic model uncovered highly significant quadratic terms for all examined parameters (Table 2), indicating complex non-linear dependencies. The likelihood of sustained spontaneous oscillations increased with $E_{\rm K}$, $E_{\rm Na}$, and $g_{\rm Na,pacemaker}$, albeit with diminishing returns, and exhibited generally convex trends (increasing up to some value, then decreasing) for $g_{\rm K,pacemaker}$, $g_{\rm K,relay}$, and $g_{\rm Na,relay}$



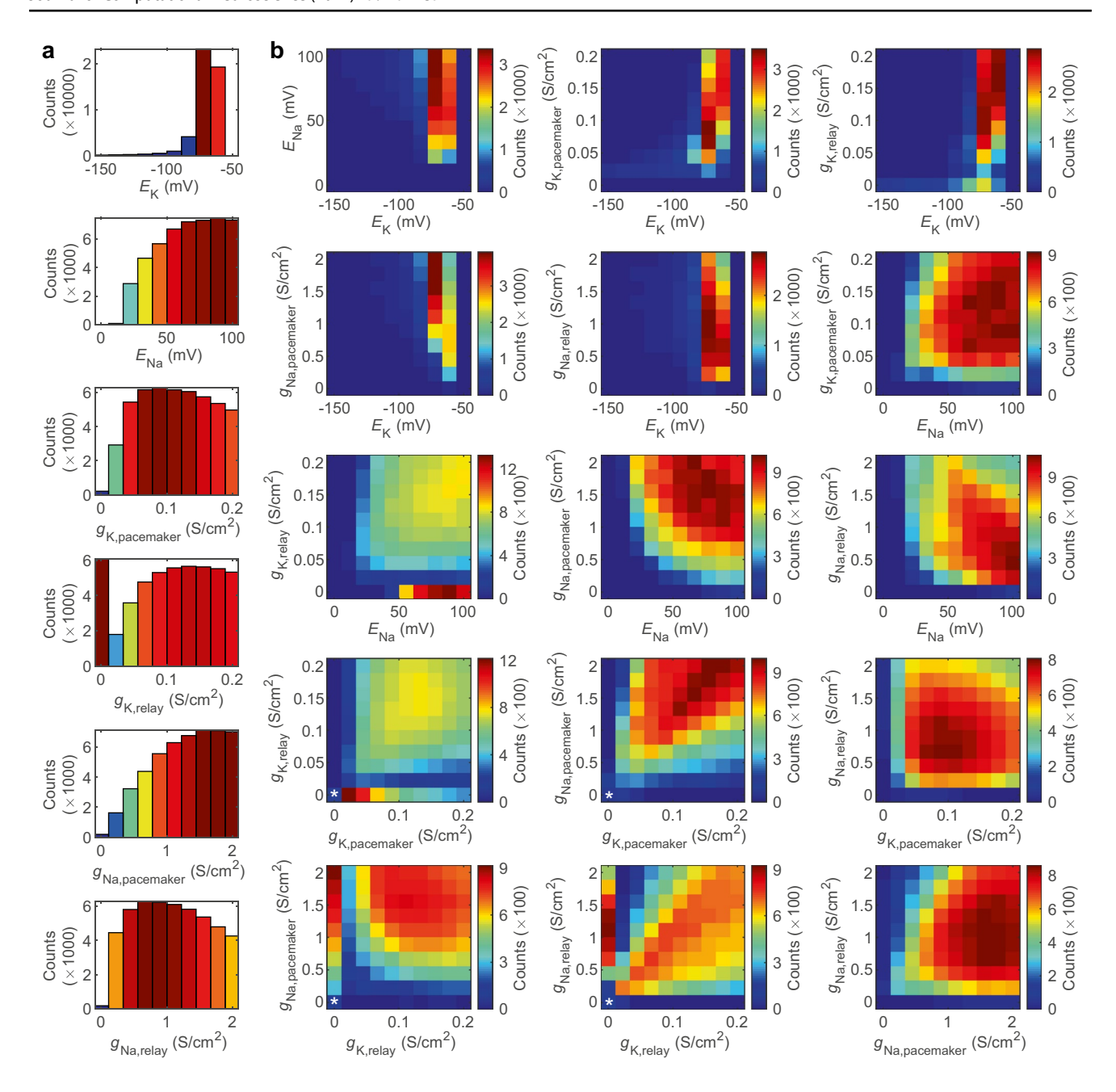


Fig. 2 Sensitivity analysis of incidence of sustained spontaneous oscillations in the Pn relative to K^+ and Na^+ equilibrium potentials (E_K, E_{Na}) and corresponding pacemaker and relay cell conductances $(g_{K,pacemaker}, g_{K,relay}, g_{Na,pacemaker}, and <math>g_{Na,relay})$. **a** univariate and **b** bivariate histograms showing absolute counts of parameter combinations resulting in sustained spontaneous oscillations at network level for each parameter value (bars in **a**), respectively for each pair of parameter values (pixels in **b**), pooled across all examined values for

remaining parameters. Counts were color coded by magnitude, separately for each subfigure; the corresponding scales are shown to the right of each plot in **b**. White asterisks in lower left plots in **b** denote parameter combinations yielding sustained spontaneous oscillations in the absence of two or more types of active ion channels, reflecting, for example, passive pacemaker or relay cell somata. Parameter sets were sampled using a uniform grid dividing each parameter range (Table 1) into 9 equal segments (total of 1 million combinations)

(negative quadratic terms in all cases) (Fig. 2a). $E_{\rm K}$ had the largest impact on Pn oscillation patterns, with absolute coefficients of linear and quadratic terms exceeding those of the remaining parameters 4.5-, respectively 7.5-fold. Sustained spontaneous oscillations were substantially more likely at

 $E_{\rm K} = -72$ and -61 mV (19–23% of tested parameter combinations) than at lower (≤ -83 mV) or higher values (50 mV) (0–4%). All pairwise interactions reached statistical significance, indicative of complex high-dimensional conditions (thresholds) for the occurrence of sustained oscillations.



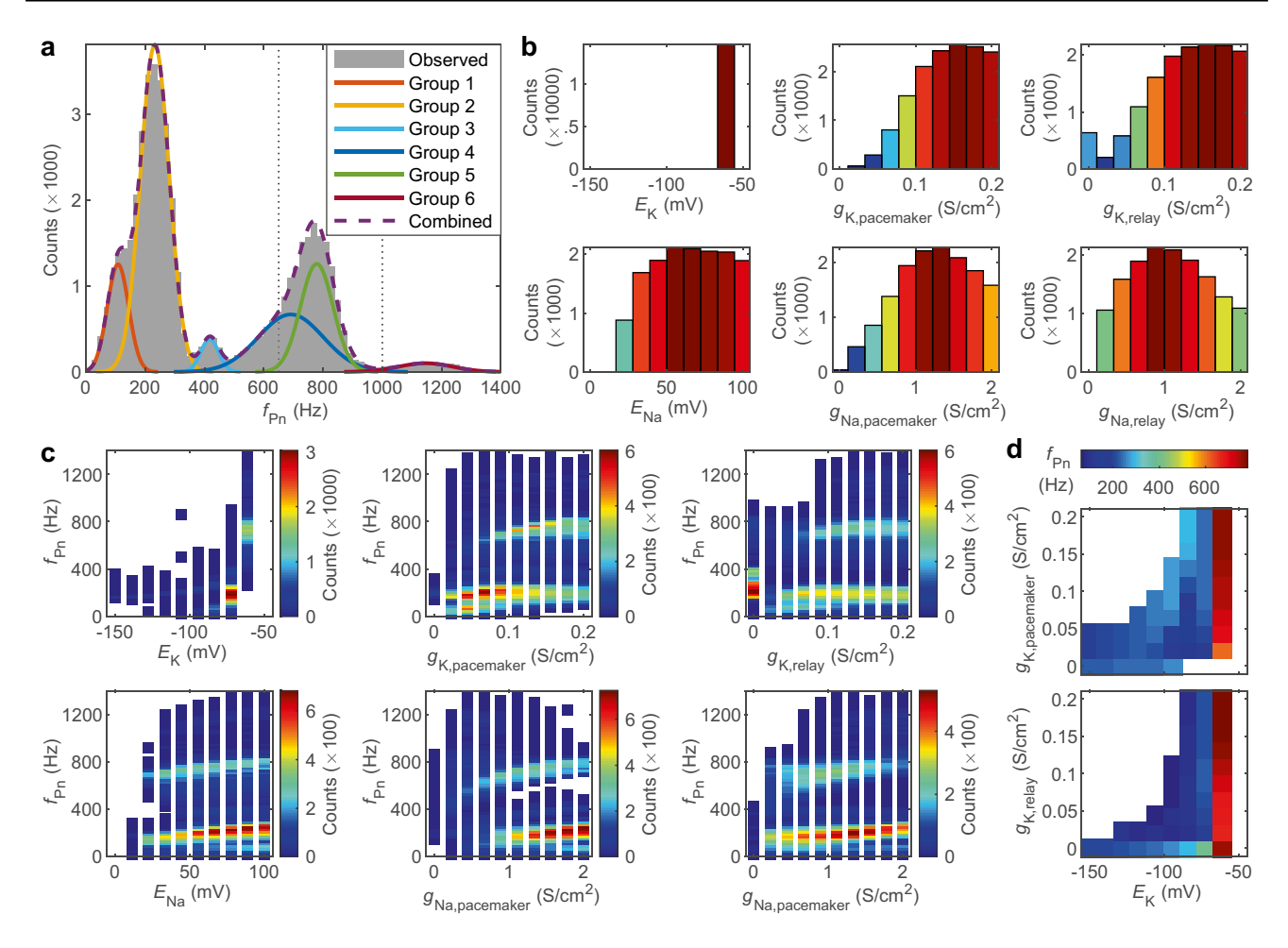


Fig. 3 Sensitivity analysis of frequency of sustained spontaneous oscillations in the Pn relative to K⁺- and Na⁺-related parameters. **a** Empirical distribution of pacemaker frequencies, $f_{\rm Pn}$ (gray bars), and its optimal Gaussian mixture fit (solid lines: individual groups; dashed line: combined probability density). Data consisted of 49,307 observations of sustained spontaneous oscillations, out of 1 million points regularly sampled from the ($E_{\rm K}$, $E_{\rm Na}$, $g_{\rm K,pacemaker}$, $g_{\rm K,relay}$) $g_{\rm Na,pacemaker}$, $g_{\rm Na,relay}$) parameter space. **b** Counts of combinations yielding sustained spontaneous oscillations with frequencies between

650–1000 Hz (physiologically relevant range; dotted vertical lines in $\bf a$ as a function of individual parameter values. Bins were color coded by magnitude, separately for each plot. $\bf c$ Scatter plots of observed Pn frequencies (rounded to the nearest multiple of 10 Hz) at different values of each individual parameter, color coded by count according to the scales shown to the right of each graph. $\bf d$ Average Pn frequency (color scale) as a function of $E_{\bf K}$ and $g_{\bf K,pacemaker}$ (top), and $E_{\bf K}$ and $g_{\bf K,relay}$ (bottom). Observations were pooled across all remaining parameters for each bin in $\bf b$, respectively for each plotted point in $\bf c$ and $\bf d$

The strongest interactions involved $E_{\rm K}$ in conjunction with $g_{\rm K,pacemaker}$, $g_{\rm Na,pacemaker}$, and $g_{\rm K,relay}$ (in this order), reinforcing the importance of $E_{\rm K}$, and of K⁺ mechanisms in general.

Follow-up analysis of Pn frequencies among those parameter combinations resulting in sustained spontaneous oscillations using a linear model uncovered broadly similar dependency patterns (Table 2). $E_{\rm K}$ had the highest impact on $f_{\rm Pn}$ (standardized regression coefficient β =1870), followed by the corresponding conductances, $g_{\rm K,pacemaker}$ and $g_{\rm K,relay}$ (β =-494 and -607, respectively). The frequency increased non-linearly with $E_{\rm K}$ (positive quadratic term coefficient) within the [-150, -61] mV range, and decreased near-linearly with $g_{\rm K,pacemaker}$ and $g_{\rm K,relay}$ (Fig. 3c). These three parameters were also involved in the two strongest interactions ($E_{\rm K} \times g_{\rm K,pacemaker}$

and $E_{\rm K} \times g_{\rm K,relay}$: $\beta = 725-850$, versus -266 to 48 for all other combinations), indicating that any decline in frequency with increasing K⁺ channel conductance can be canceled, or even reversed, at extreme $E_{\rm K}$ values (Fig. 3d). The remaining, Na⁺-related parameters had small positive impacts on the frequency ($\beta = 203-284$).

3.2 Parameter combinations associated with sustained spontaneous oscillations in the network model are confined to a single connected volume inside the parameter space

With sensitivity analysis indicating K⁺-related parameters as the chief determinants of sustained spontaneous oscillations,



Table 2 Sensitivity analysis of occurrence and frequency of sustained spontaneous oscillations with respect to $E_{\rm K}$, $E_{\rm Na}$, and the corresponding pacemaker and relay cell channel conductances. Values given are range-standardized coefficient estimates (β) \pm SE, corresponding t-statistics for contrasts versus the null hypothesis of no impact,

and overall and (between brackets) within-category ranks based on decreasing effect size (absolute value of β). All coefficients were significantly different from 0 at the 0.001 level after Bonferroni correction for multiple comparisons unless labeled otherwise; n.s., not significant

Factor		Occurrence (logistic model)			Frequency (normal model)		
		$\beta \pm SE$	t	Rank	$\beta \pm SE$	t	Rank
Linear terms	$E_{ m K}$	25.4 ± 0.17	152.4	1 [1]	1870±9.0	206.7	1 [1]
	$E_{ m Na}$	5.59 ± 0.05	106.6	7 [3]	284.2 ± 4.8	59.3	6 [4]
	$g_{ m K,pacemaker}$	-5.73 ± 0.05	-107.8	6 [2]	-494.4 ± 5.4	-91.5	5 [3]
	$g_{ m K,relay}$	-3.39 ± 0.04	-85.7	10 [5]	-606.9 ± 3.8	-159.4	4 [2]
	$g_{ m Na,pacemaker}$	5.50 ± 0.05	108.5	8 [4]	245.0 ± 3.4	72.5	8 [5]
	g _{Na,relay}	2.61 ± 0.04	64.3	14 [6]	203.1 ± 3.2	63.0	11 [6]
Quadratic terms	$E_{\rm K} \times E_{\rm K}$	-19.8 ± 0.13	-152.9	2 [1]	215.4 ± 6.5	33.0	10 [1]
	$E_{\mathrm{Na}} \times E_{\mathrm{Na}}$	-2.34 ± 0.02	-97.3	15 [3]	-54.8 ± 2.1	-26.6	14 [2]
	$g_{\mathrm{K,pacemaker}} \times g_{\mathrm{K,pacemaker}}$	-2.66 ± 0.02	-110.0	13 [2]	-33.7 ± 2.2	-15.4	21 [4]
	$g_{\text{K,relay}} \times g_{\text{K,relay}}$	-0.59 ± 0.02	-32.9	22 [6]	36.8 ± 1.2	31.3	18 [3]
	$g_{\text{Na,pacemaker}} \times g_{\text{Na,pacemaker}}$	-1.98 ± 0.02	-88.7	16 [4]	4.4 ± 1.7	n.s.2.64	26 [5]
	$g_{\text{Na,relay}} \times g_{\text{Na,relay}}$	-1.69 ± 0.02	-89.0	19 [5]	-1.5 ± 1.5	n.s1.01	27 [6]
Pairwise interactions	$E_{\rm K} \times E_{\rm Na}$	-5.40 ± 0.07	-75.0	9 [4]	-225.1 ± 6.5	-34.6	9 [4]
	$E_{\rm K} \times g_{\rm K,pacemaker}$	9.18 ± 0.08	114.9	3 [1]	724.9 ± 8.4	85.9	3 [2]
	$E_{\rm K} \times g_{\rm K,relay}$	5.93 ± 0.06	99.3	5 [3]	853.3 ± 5.7	150.0	2 [1]
	$E_{\rm K} \times g_{\rm Na,pacemaker}$	-6.13 ± 0.07	-86.6	4 [2]	-266.6 ± 4.7	-57.3	7 [3]
	$E_{\rm K} \times g_{\rm Na,relay}$	-3.35 ± 0.06	-56.7	11 [5]	-85.1 ± 4.6	-18.4	13 [6]
	$E_{\mathrm{Na}} \times g_{\mathrm{K,pacemaker}}$	1.89 ± 0.03	64.4	17 [7]	34.9 ± 2.3	15.3	20 [11]
	$E_{\text{Na}} \times g_{\text{K,relay}}$	0.48 ± 0.02	21.4	23 [13]	18.2 ± 1.8	10.4	25 [15]
	$E_{\mathrm{Na}} \times g_{\mathrm{Na,pacemaker}}$	-1.69 ± 0.03	-60.0	18 [8]	-35.3 ± 2.2	-16.2	19 [10]
	$E_{\mathrm{Na}} \times g_{\mathrm{Na,relay}}$	-1.18 ± 0.02	-48.6	21 [10]	-23.0 ± 1.8	-12.6	23 [13]
	$g_{\rm K,pacemaker} \times g_{\rm K,relay}$	-0.15 ± 0.02	-6.48	26 [14]	-46.5 ± 1.7	-27.7	16 [8]
	$g_{\text{K,pacemaker}} \times g_{\text{Na,pacemaker}}$	2.85 ± 0.03	96.0	12 [6]	48.1 ± 2.4	20.3	15 [7]
	$g_{\rm K,pacemaker} \times g_{\rm Na,relay}$	0.37 ± 0.02	15.3	25 [12]	24.7 ± 1.8	13.9	22 [12]
	$g_{\text{K,relay}} \times g_{\text{Na,pacemaker}}$	0.38 ± 0.02	17.6	24 [11]	43.7 ± 1.7	27.0	17 [9]
	$g_{\rm K,relay} \times g_{\rm Na,relay}$	1.26 ± 0.02	63.7	20 [9]	21.4 ± 1.4	15.3	24 [14]
	$g_{ m Na,pacemaker} imes g_{ m Na,relay}$	0.10 ± 0.02	4.48	27 [15]	-143.0 ± 1.7	-85.0	12 [5]

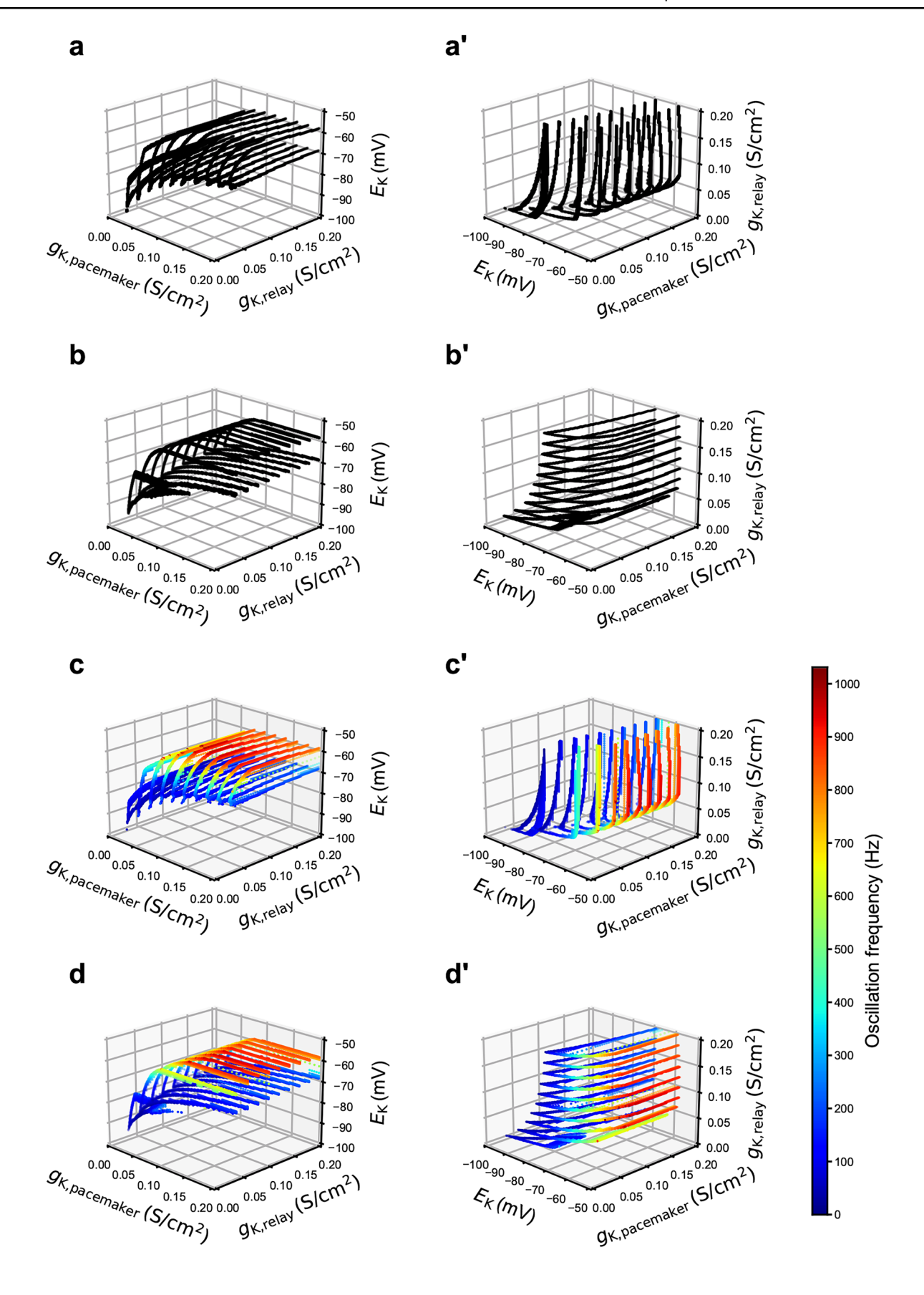
we restricted further experiments to the $(E_{\rm K},\,g_{\rm K,pacemaker},\,$ $g_{K \text{ relay}}$) three-dimensional subspace. This simplification was supported by the prohibitively high computational requirements of large-scale simulations, with 30-5,000 s per individual scenario — corresponding to over 1 week using 500 CPUs for the 1 million scenarios performed as part of the initial six-dimensional grid analysis. The surface detection algorithm described in Sect. 2.7 involved a total of 364,070 simulations of the Pn network using different parameter combinations, out of which 191,493 (52.6%) belonged to the final solution surface (see Fig. 4a, a', b, b' for selected twodimensional sections). This represents a 96.2% decrease in the number of assessed parameter sets compared to a simple grid search at the final resolution, which would have required nearly 10 million simulations, running over about 10 weeks on a high-performance cluster. While the boundaries of the volume associated with sustained oscillations depended on

all three parameters, frequencies seemed to depend only on $E_{\rm K}$ (Fig. 4c, c', d, d').

3.3 The frequency and amplitude of sustained spontaneous oscillations in the network model and in isolated pacemaker and relay cells show similar dependence on E_K

To contrast the effect of $E_{\rm K}$ on the frequency and amplitude of sustained spontaneous oscillations between the network model and isolated pacemaker and relay cells, we simulated these 3 models over an evenly distributed grid of $E_{\rm K}$ values \in [-75, -50] mV with step size 0.5 mV, while fixing somatic $g_{\rm K}$ to 0.1 S/cm² for both cell types (all other parameter values as listed in Table 1). Both the network and isolated cell models exhibited sustained spontaneous oscillations within strongly overlapping parts of







<Fig. 4 Application of bisection and surface continuation algorithm to occurrence of sustained spontaneous oscillations in the Pn as a function of K⁺-related parameters. **a**, **a'**, **b**, **b'** Points sampled from the three-dimensional surface across which the simulated network transitions between sustained spontaneous oscillations and the absence of such oscillations. **c**, **c'**, **d**, **d'** Points corresponding to non-zero spontaneous oscillation frequencies, color-coded according to the frequency scale shown on the right. Cross sections of the surface are plotted at fixed $g_{K,pacemaker}$ (**a**, **a'**, **c**, **c'**) and fixed $g_{K,relay}$ (**b**, **b'**, **d**, **d'**) values within the [0, 0.2] S/cm² range, with evenly distributed steps of 0.02 S/cm² and including boundary points. Objects in **a/a'**, **b/b'**, **c/c'**, and **d/d'** are identical but shown from different view angles for each pair

this $E_{\rm K}$ range (Fig. 5). The oscillation frequency of the network appeared to be a weighted average (by population size) of that of isolated pacemaker and relay cells (Fig. 5a). Moreover, oscillation amplitudes in the network (averaged over cell populations) and isolated cell models closely followed each other for both pacemaker and relay cells (Fig. 5b). Across both network and isolated cell models, oscillation frequency increased almost linearly with $E_{\rm K}$ (Fig. 5a), while amplitude decreased super-linearly with increasing $E_{\rm K}$ (Fig. 5b).

3.4 The frequency and amplitude of sustained spontaneous oscillations in isolated cells and Hodgkin-Huxley equations show similar dependence on E_K

Bifurcation analyses of Hodgkin-Huxley equation models of pacemaker and relay cell somata (Fig. 6 top) yielded amplitudes (Fig. 6 middle) and frequencies (Fig. 6 bottom) similar to those of isolated pacemaker and relay cell models (Fig. 5). While the frequency curve of the Hodgkin-Huxley pacemaker cell deviated visibly in level but not trend from that of an isolated pacemaker cell, there were no noticeable differences for relay cells (Fig. 5a). In contrast, amplitude curves of Hodgkin-Huxley equation and isolated cell models exhibited only minor differences in both cell types (Fig. 5b). Note that, although sustained spontaneous oscillations cover wider $E_{\rm K}$ ranges for Hodgkin-Huxley equation models, detection of sustained spontaneous oscillations via numerical simulations can fail at low frequencies and small amplitudes. The former is caused by simulating over a limited interval of 100 ms, while the latter is caused by limitations of NEURON's action potential detection algorithm.

3.5 Frequency decrease with increasing $E_{\rm K}$ results mainly from lengthening of the refractory period

To gain insights into how different ion channels contribute to the generation of action potentials, we inspected the dynamics of V, $g_{\rm K}$, and $g_{\rm Na}$ over a single oscillation period at various $E_{\rm K}$ values. While there are natural differences in amplitude, membrane potentials and channel conductances of pacemaker (Fig. 7 left) and relay (Fig. 7 right) cells showed very similar waveforms — albeit at shifted $E_{\rm K}$ values. As $E_{\rm K}$ increased, the peak $g_{\rm K}$ value generally decreased (Fig. 8 top) while its phase increased (Fig. 8 bottom), which was paralleled by an increasingly incomplete closure of K⁺ channels (Fig. 8 top). In contrast, $g_{\rm Na}$ peaks were subject to only minor shifts (Fig. 8 bottom), while their amplitude sharply decreased with $E_{\rm K}$ after a small initial increase (Fig. 8 top).

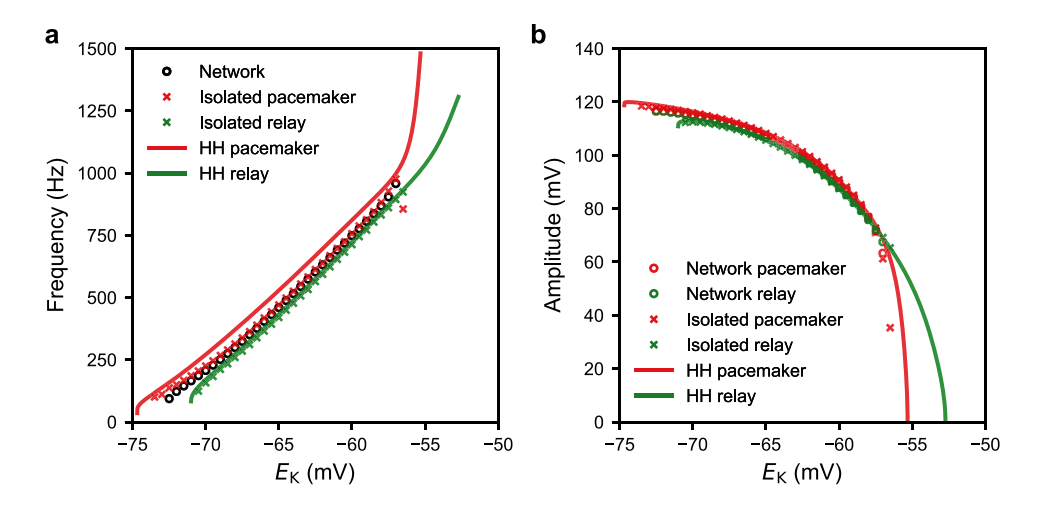
To better visualize the effect of $E_{\rm K}$ on these waveforms and the timing of conductance peaks relative to the peak of V, we plotted the K⁺ and Na⁺ channel conductances with respect to $E_{\rm K}$ and phase (Fig. 9) or absolute time (Fig. 10). Although the temporal dynamics of K⁺ channel opening showed dependence on $E_{\rm K}$ when time was normalized to the oscillation period (Fig. 9 top), plotting $g_{\rm K}$ with respect to $E_{\rm K}$ and absolute time (Fig. 10 top) revealed that the timing of K⁺ channel opening remained mostly constant. A similar pattern could be observed for Na⁺ channels, whose opening/closing dynamics changed only slightly in absolute time, while the time-period of oscillation decreased rapidly with respect to $E_{\rm K}$ (Fig. 10 bottom). Consequently, the change in time-period was mostly due to changes in the refractory period.

4 Discussion

The present investigation has two main achievements. The first is the construction of a model of the Pn neural network capable of generating simulated sustained spontaneous oscillations under a variety of conditions and at similar frequencies to those produced by the biological system. This was necessary since previous models, including one from our group, were only able to generate oscillatory activity at the whole network level after current injection — though some did succeed in producing sustained spontaneous oscillations by isolated pacemaker cells (Lucas et al., 2019; Moortgat et al., 2000b; Shifman et al., 2020; Zupanc et al., 2019). The second accomplishment of the present study is the comprehensive exploration of the parameter space of this novel model, with particular emphasis on the role of active K⁺ conductances and $E_{\rm K}$ (as a proxy for $[{\rm K}^+]_{\rm o}$). In the following sections, we will discuss these outcomes and compare them with both theoretical and experimental findings obtained through the study of the Pn of A. leptorhynchus and of other neural systems and organisms.



Fig. 5 Dependence on E_{K} of a frequency and b amplitude of sustained spontaneous oscillations in the Pn network model (circles), isolated pacemaker and relay cell models (crosses), and the Hodgkin-Huxley (HH) models of pacemaker and relay cell somata (solid lines), with parameters fixed according to Table 1. Results corresponding to pacemaker and relay cells are shown in red and green, respectively. Note that frequencies of these two cell types were identical in the network model

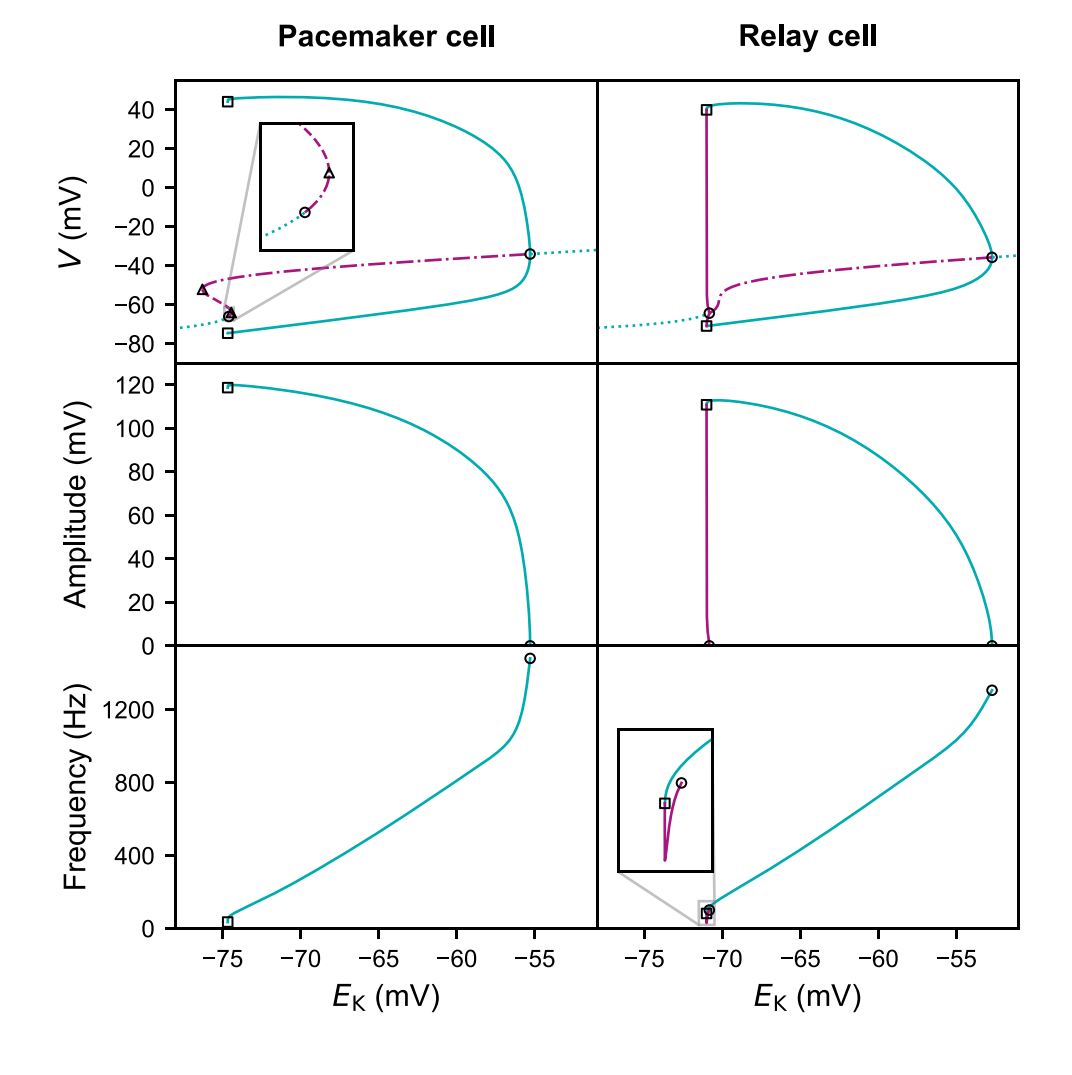


4.1 General conditions for sustained spontaneous oscillations

Large scale assessment of the ($E_{\rm K}$, $E_{\rm Na}$, $g_{\rm K,pacemaker}$, $g_{\rm K,relay}$, $g_{\rm Na,pacemaker}$, $g_{\rm Na,relay}$) space revealed an array of K⁺- and

 Na^+ -related parameters resulting in sustained spontaneous oscillations in the Pn. While oscillatory patterns proved relatively rare overall (5% of the explored parameter combinations), they could be observed for $E_\mathrm{K} < -50$ mV, $E_\mathrm{Na} > 0$ mV, and all tested pacemaker and relay cell K^+ and

Fig. 6 Bifurcations (top row), oscillation amplitude (middle row), and oscillation frequency (bottom row) in the Hodgkin-Huxley equations with respect to $E_{\rm K}$. Model parameters for pacemaker (left column) and relay (right column) cell somata were set according to Table 1. Teal and purple curves represent stable and unstable invariant manifolds, respectively, projected onto the $E_{\rm K}$ – V plane. Dotted, dashed, and dash-dotted curves correspond to equilibria whose Jacobians have 0, 1, and 2 unstable roots, respectively. Solid curves mark the maximum and minimum V values of limit cycles. Triangle, circle, and square markers indicate saddle-node, Hopf, and fold limit cycle bifurcation points, respectively. Insets show the boxed areas at higher magnification





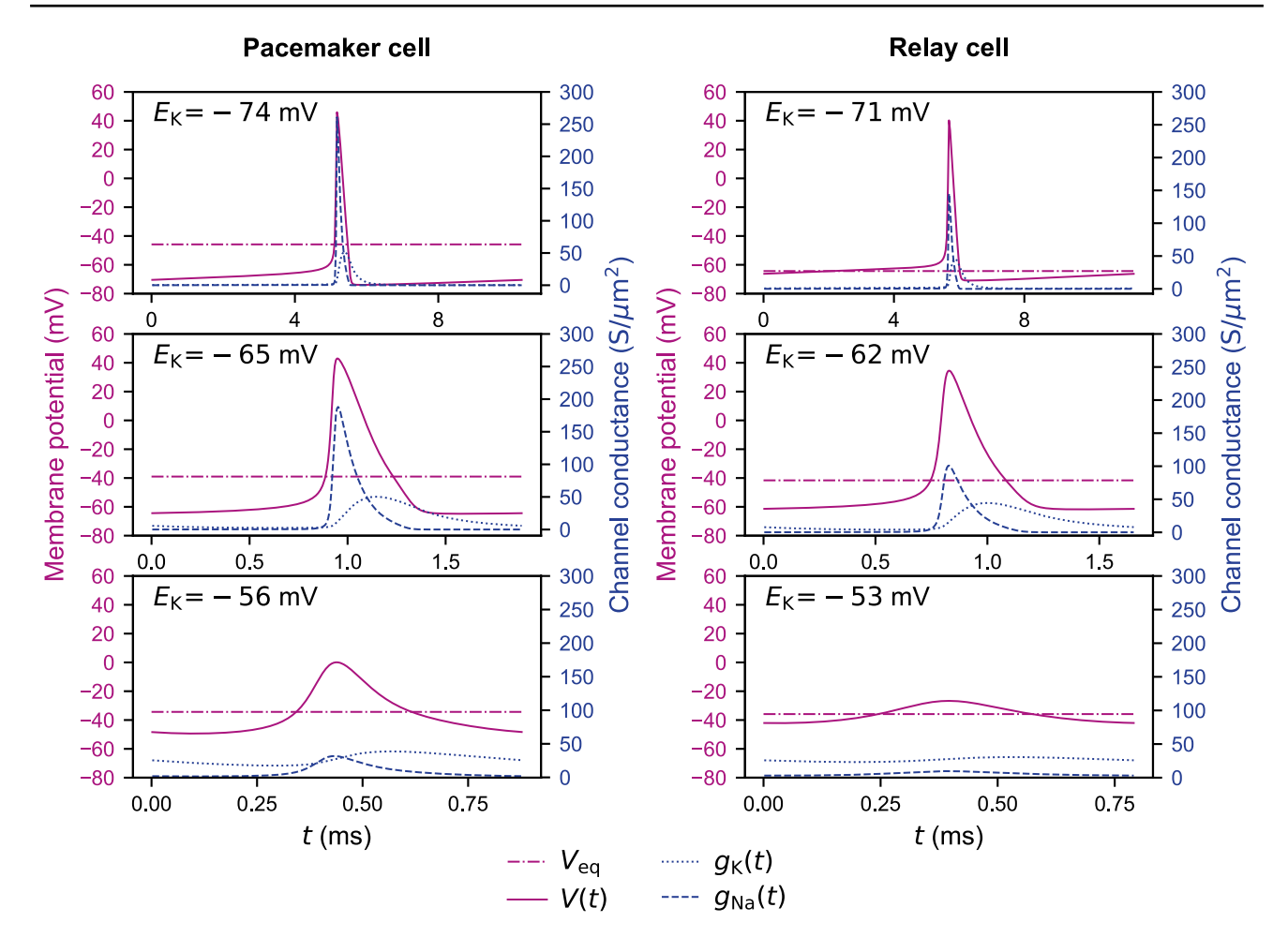


Fig. 7 Membrane potential (purple, left vertical axis) and conductance of voltage-gated K^+ and Na^+ channels (blue, right vertical axis) during sustained spontaneous oscillations in the Hodgkin-Huxley equations for pacemaker (left column) and relay (right column) cell somata at various E_K values (indicated at the top left of each subfigure). Model parameters for pacemaker and relay cell somata were

fixed according to Table 1. Solid and dash-dotted purple lines represent V(t) and its Hodgkin-Huxley equilibrium, $V_{\rm eq}$, respectively. Dashed and dotted blue lines denote $g_{\rm Na}(t)$ and $g_{\rm K}(t)$, respectively. All curves are plotted for one oscillation period T, shifted such that V(t) reaches its peak at t = T/2

Na⁺ channel conductance values (Fig. 2a). Statistical analysis revealed non-linear dependencies for, and significant pairwise interactions between, all included parameters, indicating non-trivial conditions for spontaneous Pn oscillations (Table 2, Fig. 2b).

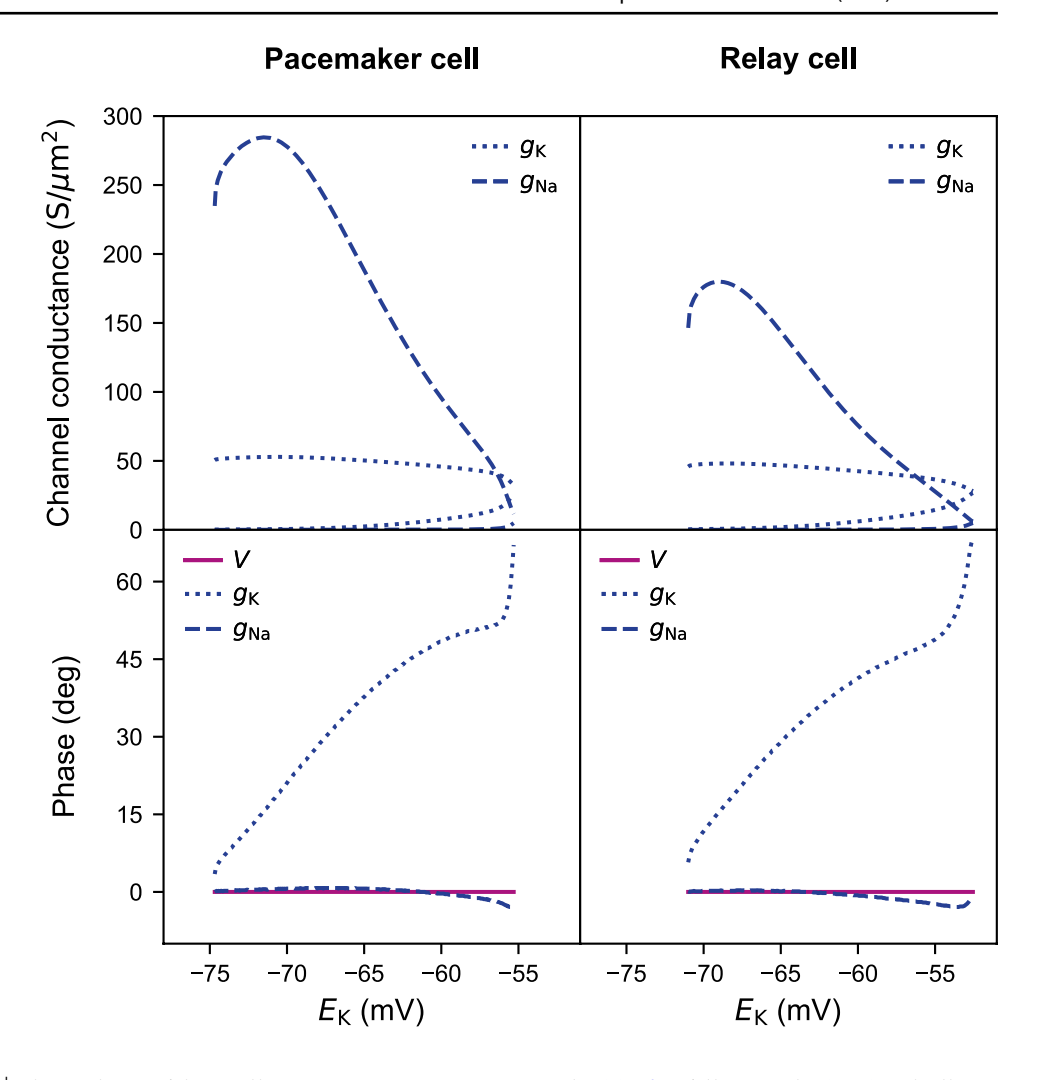
Most importantly, our analysis identified $E_{\rm K}$ as the critical determinant of sustained spontaneous oscillations in the Pn (linear and quadratic terms with the largest range-standardized coefficients). Network-wide synchronized firing was substantially more prevalent at $E_{\rm K}$ values \in [-75, -60] mV (roughly 20% of the tested parameter combinations) compared to the [-150, -80] mV range (0-4%) or at -50 mV (0%). The criticality of K⁺-related mechanisms was reinforced by the dominant interaction effects, which involved $E_{\rm K}$ in conjunction with, among others, the two corresponding conductances, $g_{\rm K,pacemaker}$ and $g_{\rm K,relay}$; as well as by the identification of similarly large main and interaction

effects involving the same three parameters when analyzing the Pn frequency (Table 2). Other parameters with large effect sizes included $g_{\rm K,pacemaker}$ (0.2% at 0 S/cm² versus 4.9–6.3% at > 0.04 S/cm²) and $g_{\rm Na,pacemaker}$ (0.2% at 0 S/cm² versus 3.2–6.8% at > 0.4 S/cm²), underlying the importance of active conductances on pacemaker cells.

Interestingly, our exhaustive exploration of the considered parameter space — expanding well beyond values recorded in this or other vertebrate species, to avoid any anchoring biases — also uncovered evidence of sustained spontaneous oscillations of the Pn in the absence of active conductances on relay or pacemaker cells. Out of the nearly 50,000 parameter sets found to result in synchronous sustained firing at network level, 0.1% involved passive pacemaker cell somata, 0.2% featured passive relay cell somata (i.e., of the type considered in prior modeling research by our group and others (Moortgat et al., 2000b; Zupanc et al., 2019)), while



Fig. 8 Channel conductance extrema (top row) and conductance maxima phases relative to the action potential peak (bottom row) as a function of $E_{\rm K}$ during sustained spontaneous oscillations in the Hodgkin-Huxley equations for pacemaker (left column) and relay (right column) cell somata. Model parameters were set according to Table 1. Dashed and dotted blue lines denote maximum and minimum values (top) and phases of the maximum value (bottom) of $g_{Na}(t)$ and $g_{K}(t)$, respectively. Solid purple lines on the bottom row mark the phase of the peak value of V



0.4% did not require active K⁺ channels on either cell type (Fig. 2b). These candidate solutions featured low $E_{\rm K}$ values (\leq -106 mV) or high $E_{\rm Na}$ values (\geq 67 mV), and yielded Pn frequencies significantly lower than those measured in live fish — between 14–426 Hz at 27 °C in the present simulations, compared to a minimum EOD frequency of 671 Hz at 26 °C (Zupanc et al., 2014), which is equivalent to 702 Hz at 27 °C (using a Q₁₀ of 1.56; (Zupanc et al., 2003)).

Consistent with this frequency discrepancy between simulation outputs and the modeled biological system, application of the Nernst equation indicates that these theoretical solutions are likely not physiologically relevant. Assuming an intracellular potassium concentration, $[K^+]_i$, in pacemaker and relay cells of 140 mM, as typically found in mammalian neurons (Lodish et al., 2000), E_K values of -106 to -150 mV would result in $[K^+]_0$ of 0.4–2.3 mM — generally lower than the values of 1.7–3.6 mM determined by various methods in fish (Nilsson et al., 1993; Rice & Nicholson, 1988), and of around 3 mM measured in the mammalian brain (Lux & Neher, 1973; Moody et al., 1974; Prince et al., 1973). Similarly, assuming commonly used values for intracellular Na⁺ concentration of 10–15 mM

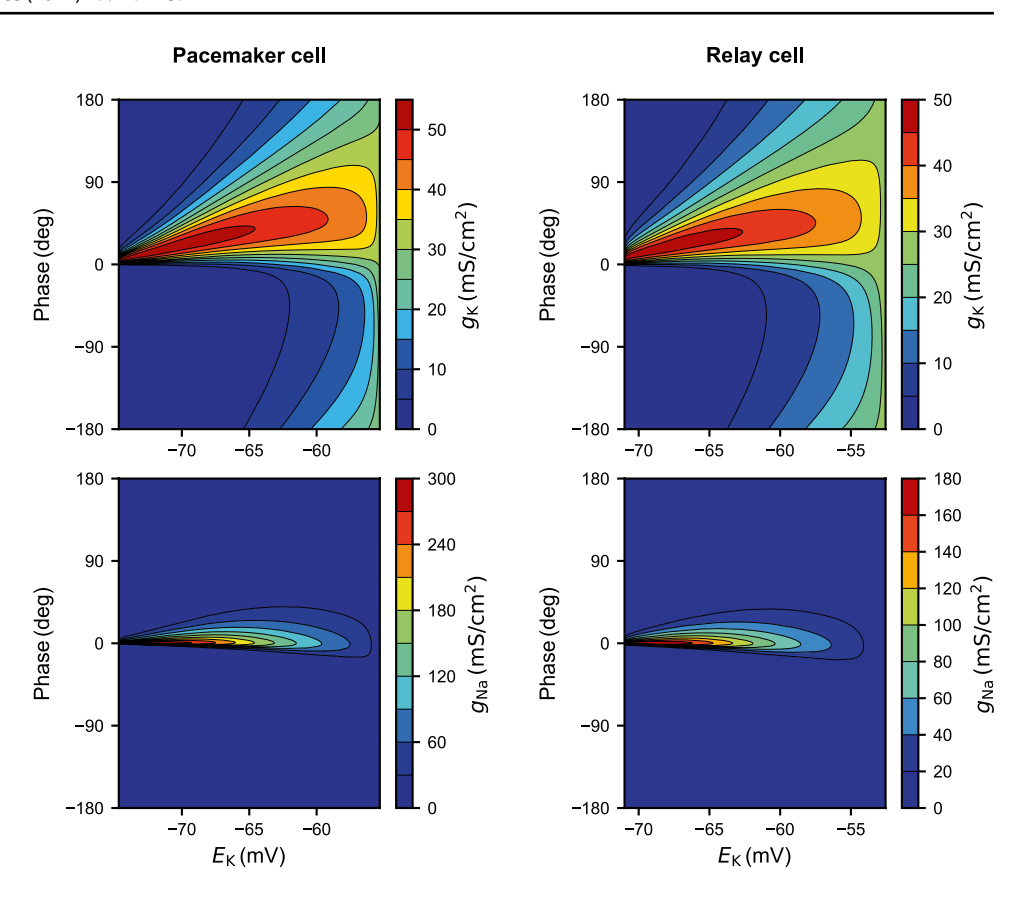
(e.g., Petracca et al., 2016; Ridley et al., 2018; Thulborn et al., 1999), $E_{\rm Na}$ values of 100 mV and 67 mV would correspond to an extracellular concentration of 478–717 mM and 134–200 mM, respectively, i.e., generally larger than the commonly assumed value of 140 mM. In future studies, *in vitro* testing of such extreme conditions could help identify pacemaker and relay conductances and further refine the present models.

4.2 Active conductances in the relay cell soma

The present study is, to our knowledge, the first to develop a model of the Pn network that can produce sustained spontaneous oscillations in the absence of current injection. A critical step towards this goal was the addition of g_{Na} and g_{K} to the somata of relay cells, which were absent in previous models of the Pn network (Lucas et al., 2019; Moortgat et al., 2000b; Zupanc et al., 2019). While isolated pacemaker cells (with the somatic compartment containing active K⁺ and Na⁺ channels) exhibited spontaneous oscillations (Zupanc et al., 2019), in networks of interconnected pacemaker and relay cells such activity could be simulated



Fig. 9 Conductance of voltagegated channels during sustained spontaneous oscillations in the Hodgkin-Huxley equations, with model parameters for pacemaker (left column) and relay (right column) cell somata set according to Table 1. Magnitudes of K+ (top row) and Na⁺ (bottom row) conductances are color coded according to the scales displayed to the right of each subfigure. Values are plotted against $E_{\rm K}$ and phase (time normalized to one oscillation period). Note that conductance curves in Fig. 7 are vertical slices of the respective subfigures shown here



only by injection of a constant current of 1 nA (Lucas et al., 2019; Moortgat et al., 2000b; Zupanc et al., 2019).

The deliberate omission of active conductances in somata of relay cells in prior modeling studies was allegedly based on "experimental observations of low-amplitude spikes in the somata compared with those in the axon, an effect seen in both cell types [pacemaker and relay] (Dye & Heiligenberg, 1987) but most pronounced in the relay cells (pers. observation)" (Moortgat et al., 2000b). Whereas we were not able to evaluate the validity of the latter statement, we carefully reviewed the Dye and Heiligenberg (1987) paper for possible reporting of experimental evidence supporting the former statement. However, we could not find any mention of reduced amplitudes of spikes generated by pacemaker or relay cell somata, compared to spikes recorded from axons. Moreover, the present sensitivity analysis indicated that relay cells without active conductances can only generate oscillations with frequencies well below biologically observed value ranges (cf. Sects. 3.1 and 4.1). We, therefore, conclude that there is no direct or indirect evidence for active conductances being absent from the somata of relay cells.

This conclusion is in line with a wealth of studies in which the subcellular distribution of voltage-gated Na⁺ and K⁺ channels was determined (for reviews see Lai & Jan, 2006; Trimmer & Rhodes, 2004). For example, the voltage-gated Na⁺ channels Na_v1.1, Na_v1.3, and Na_v1.6 are all

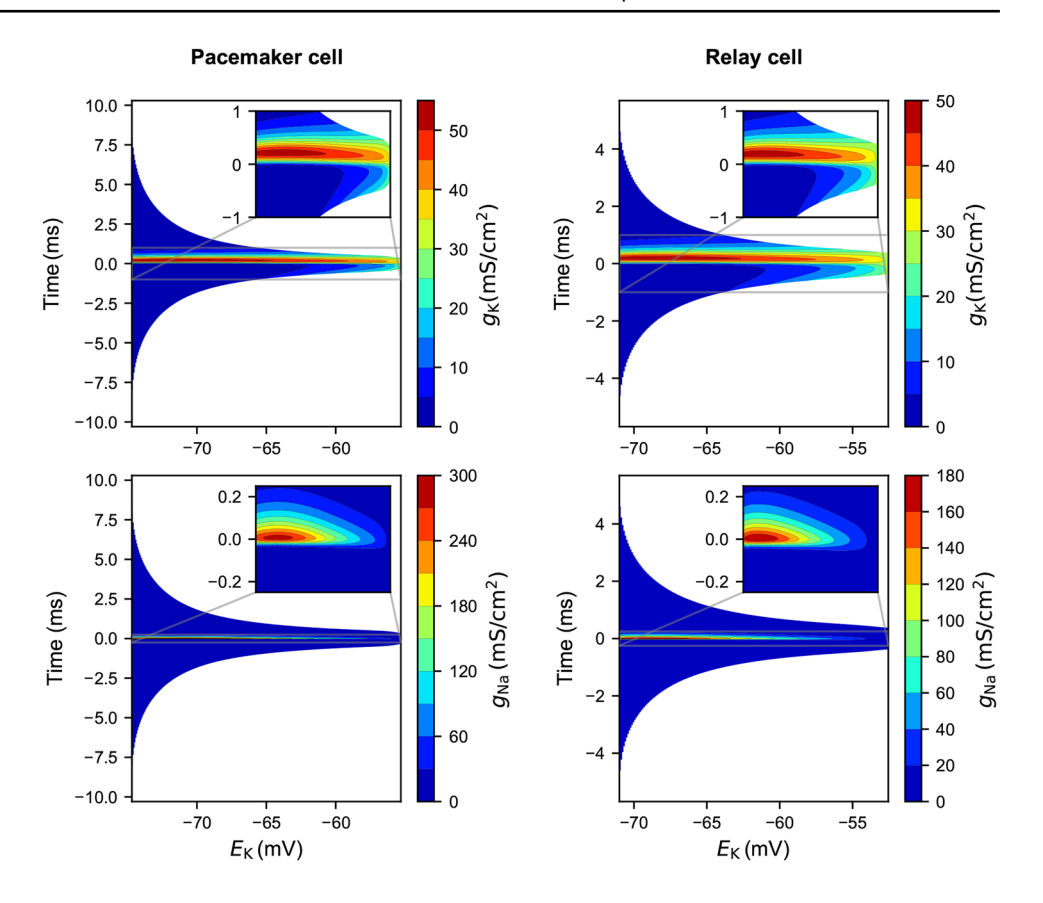
present in somata of various neuronal types in the CNS, whereas $Na_v1.2$ is even localized predominantly on cell bodies and dendrites. Similarly, the voltage-gated K^+ channel $K_v2.1$ appears restricted to somata and proximal dendrites but absent from the axons and nerve terminals, while K_v3 channels have been found on somatodendritic regions in addition to axons and presynaptic terminals. A similar finding was made in *A. leptorhynchus* using antibodies directed against an amino acid sequence specific for the $K_v3.1$ channel in this species. This study showed that the AptKv3.1 protein is highly concentrated in somata and proximal dendrites of pyramidal neurons of the electrosensory lateral line lobe (Deng et al., 2005).

4.3 Effect of [K⁺]_o on neural activity

Simulations using our Pn network model identified $E_{\rm K}$ as a critical determinant of the frequency and amplitude of sustained spontaneous oscillations generated by pacemaker and relay cells. This finding was independent of whether these cells were isolated from one another or connected through gap junctions and, in the latter configuration, of whether the somata of either relay cells or pacemaker cells — but not both — lacked active conductances. These results extend previous research from our laboratory using a model in which active conductances were absent from



Fig. 10 Conductance of voltage-gated channels during sustained spontaneous oscillations in the Hodgkin-Huxley equations, with model parameters for pacemaker (left column) and relay (right column) cell somata set according to Table 1. Magnitudes of K+ (top row) and Na⁺ (bottom row) conductances are color coded according to the scales shown to the right of each subfigure. Data are plotted for a single oscillation period against $E_{\rm K}$ and time, with the latter measured relative to the location of the peak value of V. For improved visibility, areas corresponding to sharp changes in conductance are shown magnified in the insets



relay cells but present on pacemaker cells. This prior study produced similar results, but observations of sustained spontaneous oscillations were restricted to isolated pacemaker cells (Zupanc et al., 2019). To examine the effect of $E_{\rm K}$ on firing patterns at the network level using this earlier model, it was necessary to induce oscillations by injection of a constant current of 1 nA into the relay cell somata (see 4.2, above). As in the current study, the frequency of both spontaneous oscillations of isolated pacemaker cells and induced oscillations of the Pn network was strongly positively correlated with $E_{\rm K}$, an effect that was paralleled by a decrease in oscillation amplitude with increasing $E_{\rm K}$.

According to the Nernst equation, changes in $E_{\rm K}$ can be exclusively attributed to changes in $[{\rm K}^+]_{\rm o}$, assuming $[{\rm K}^+]_{\rm i}$ remains constant. Studies in a variety of organisms, including mammals (Lux & Neher, 1973; Moody et al., 1974; Prince et al., 1973) and fish (Nilsson et al., 1993; Rice & Nicholson, 1988), have suggested that $[{\rm K}^+]_{\rm o}$ is very similar across species and taxa, usually ranging between 2–3 mM. Increases in $[{\rm K}^+]_{\rm o}$ from resting levels typically occur as a result of action potential generation, with size estimates varying from 0.01–0.02 mM in the mesencephalic reticular formation of rats (Syková et al., 1974) to 0.8 mM in ganglia of the CNS of the medicinal leech (Baylor & Nicholls, 1969) and 1.6 mM in the giant axons of *Loligo* (Frankenhaeuser & Hodgkin, 1956) for

a single action potential. Therefore, naturally occurring neural activity, e.g., resulting from sensory stimulation, electrical stimulation at physiological strength, or brain state transitions, generally leads to increases in $[K^+]_o$ of a few mM. In pathological conditions, such as seizures and ischemia, and after strong electrical stimulation, $[K^+]_o$ may rise by as much as 85 mM above baseline levels (for review see Rasmussen et al., 2020).

Correspondingly, any increase in [K⁺]_o results in a proportional depolarization of V, as E_K becomes less negative. This reduction in the difference between the resting potential V_{rest} and the threshold potential at which voltage-gated Na⁺ channels are activated increases neuronal excitability (Wang et al., 2012). Application of the Goldman-Hodgkin-Katz equation predicts that an increase in $[K^+]_0$ by 2 mM shifts V_{rest} of a 'standard' mammalian neuron by approximately 3 mV towards less negative values. Experimental evidence also supports this theoretical prediction that even minute increases in [K⁺]_o can lead to significant depolarization of neurons. In a slice preparation of the striatum of mice, an increase in $[K^+]_0$ of the bath solution by 1.5 mM resulted in an approximately 6 mV depolarization of medium spiny neurons (Tong et al., 2014). Similarly, raising [K⁺]₀ by 0.7 mM depolarized cortical L2/3 pyramidal neurons in slices of the mouse cortex by 4 mV (Rasmussen et al., 2019).



Changes in intrinsic excitability induced by $[K^+]_o$ can result in various modulations of oscillatory firing modes of neurons. An experimental increase of $[K^+]_o$ from 4 to 6 mM induced a switching of interneurons (thought to be part of the locomotor network) in the spinal cord of neonatal rats from tonic spiking to a bursting mode (Brocard et al., 2013). In cultured networks of cortical neurons of rats, an increase of $[K^+]$ in the culture medium from 1.4 to 5.6 mM resulted in a rise in bursting frequency (Canepari et al., 1997). In cultured cortical neurons of mice, at $[K^+]$ of 1.5 mM, irregular spike firing, interspersed by long periods of silence, was observed. At 3.0 mM $[K^+]$, sporadic network burst firing occurred, and at 5.4 mM $[K^+]$ the burst activity increased further. When $[K^+]$ was further raised to 8.0 mM, the activity pattern changed to tonic spike firing (Golbs et al., 2011).

Similar state transitions have been predicted using a computational model of a neocortical circuit with extracellular K^+ dynamics (Fröhlich et al., 2006). At $[K^+]_o = 4.85$ mM, the simulated neuron switched from a resting state to tonic firing. At $[K^+]_o$ ranging from 5.45–6.35 mM, bistability occurred between this tonic firing and a new mode, slow bursting. At $[K^+]_o$ between 6.35–9.45 mM, slow bursting was exhibited as the only stable state. At $[K^+]_o = 9.46$ mM, a new stable state distinguished by depolarization at V = -26.3 mV appeared, which coexisted with the slow bursting state before it became the only stable state at $[K^+]_o = 10.05$ mM.

The effect of [K⁺]_o on neural activity patterns is particularly striking when neurons are exposed to excessively high concentrations of this ion species. For example, blockade of gap junctions caused severe impairment of [K⁺]₀ buffering in the locust metathoracic ganglion, increasing the vulnerability of neural tissue to spreading depression induced by Na⁺/K⁺-ATPase inhibition (Spong & Robertson, 2013). In layers II/III of the somatosensory cortex of mice, impairment of astrocytic K⁺ clearance through inhibition of K⁺ uptake by K_{ir}4.1 channels or through selective blockade of the gap-junction protein connexin-43 increased network excitability and resulted in high-power network oscillations over a wide range of frequencies. At the cellular level, increases in [K⁺]₀ led to modulation of oscillatory activity of individual neurons (Bellot-Saez et al., 2018). Under pathological conditions, similar network hyperexcitability might contribute to the etiology of epileptic seizures (for review see Bellot-Saez et al., 2017).

Taken together, the above studies suggest that the effects of $[K^+]_o$ modulation on neural activity are complex and depend on a variety of factors, including the specific brain system and the magnitude of the change. In the current modeling study, we examined the effect of E_K , as a proxy for $[K^+]_o$ (assuming $[K^+]_i$ remained constant), on the frequency of sustained spontaneous oscillations of the Pn network and neurons comprising it. These simulations were designed to

model frequency shifts similar to those occurring during development of the sexually dimorphic EOD of *A. leptorhynchus*. Our results predict that a change in $E_{\rm K}$ of only 2.5 mV, from –60.2 mV to –57.7 mV, is required to increase $f_{\rm Pn}$ from 737 to 892 Hz (median $f_{\rm EOD}$ in adult females and males, respectively (Zupanc et al., 2014)). Assuming $[{\rm K}^+]_{\rm i}$ in *A. leptorhynchus* pacemaker and relay cells is similar to mammalian neurons, i.e., 140 mM (Lodish et al., 2000), application of the Nernst equation shows that an increase of $[{\rm K}^+]_{\rm o}$ from a baseline level of 13.2 mM by as little as 2.3 mM suffices to change $f_{\rm Pn}$, and thus $f_{\rm EOD}$, from values typical of females to values characteristic of males.

4.4 Role of astrocytic syncytium in the clearance of extracellular K⁺

Among all central pattern generators known, the *A. leptorhynchus* Pn is unsurpassed in both its extremely high output frequency and its duty cycle. The generation of EODs with characteristics of adult individuals starts at approximately 1 year of age (Kirschbaum, 1983) and continues, with a 100% duty cycle, until end of life. With an average EOD frequency of 700–1000 Hz, every single pacemaker or relay cell within the Pn generates 22–32 billion action potentials each year, or more than 130 billion spikes over the estimated 7-year lifespan of the fish. These figures give a first indication of the magnitude of continuously occurring repolarizing efflux of K⁺ ions from these cells into the interstitial space.

Elevated levels of extracellular K⁺ cause depolarization of neuronal membranes, which, as detailed above in Sect. 4.3, may result in uncontrolled changes in excitability and, thus, compromised neuronal function. To avoid such negative effects, mechanism(s) that tightly regulate the homeostatic set-point for K⁺ in the interstitial space are paramount. Given the immense amount of K⁺ released during Pn oscillations, it is highly unlikely that activity of the neuronal Na+/K+-ATPase alone is sufficient to remove K⁺ ions from the extracellular space and cycle them back to pacemaker and relay cells. Instead, as suggested by the large number of astrocytes in the Pn and their close spatial association with these neuron types (Sîrbulescu et al., 2014), buffering and redistribution of K⁺ might be mediated at least partially, and probably predominantly, by these glia. Research on other neural systems has implicated both an (active) energy-dependent pathway involving a glial isoform of Na⁺/K⁺-ATPase and (passive) diffusion through K⁺ channels as mechanisms underlying K⁺ uptake by astrocytes (for reviews see Verkhratsky & Nedergaard, 2018; Walz, 2000). Subsequently, redistribution of K⁺ from sites of elevated concentration to sites of lower concentration takes place within the astrocytic syncytium, a process facilitated by the extensive gap-junction coupling between individual astrocytes and the resulting syncytial isopotentiality (Kiyoshi & Zhou, 2019; Ma et al., 2016).



4.5 Role of astrocytic syncytium in modulation of neural activity induced by changes in [K⁺]_o

In addition to its hypothesized function as a sink for K^+ ions released during the repolarization phase of neuronal firing, the astrocytic syncytium surrounding pacemaker and relay cells has also been implicated in the development and maintenance of the sexually dimorphic $f_{\rm EOD}$ (Zupanc, 2017, 2020; Zupanc et al., 2014, 2019). Both the surface area of pacemaker and relay cells covered by astrocytes and the gap-junction coupling strength between individual cells within the syncytium are larger in females than in males (Zupanc et al., 2014). According to the proposed hypothesis, these characteristics manifest in females through a persistently elevated K^+ astrocytic buffering capacity, which, in turn, leads to reduced $[K^+]_0$ in females compared to males.

Our simulations predict that the difference in f_{EOD} between females and males is largely caused by a shift in the minimum K⁺ conductance over one oscillation period. This minimum is close to $0 \text{ S/}\mu\text{m}^2$ at lower E_K values but displays elevated levels, converging to the corresponding maximum, at higher $E_{\rm K}$ values (Fig. 8 top). This shifts $V_{\rm rest}$ from more negative values in females to less negative values in males, which has two major consequences: (i) the gap to the threshold potential at which voltage-gated Na⁺ channels are activated and action potentials are initiated is narrowed; and (ii) the difference between V_{rest} and $E_{\text{L}} = -70 \text{ mV}$ is increased, which elevates the leak current level, thereby decreasing the refractory period (Fig. 10). The former leads to a rise in frequency by increasing the excitability of pacemaker and relay cells, whereas the latter contributes to this effect by shortening the oscillation period.

In the present simulations, changes in $f_{\rm Pn}$ induced by manipulation of $E_{\rm K}$, e.g., as a result of alteration of astrocytic K⁺ buffering and thus of $[{\rm K}^+]_{\rm o}$, were paralleled by opposite changes in oscillation amplitude. In biological systems, a similar negative effect of increased $[{\rm K}^+]_{\rm o}$ on the amplitude of action potentials has been reported previously for a variety of neural systems and organisms, including the ommatidia of the lateral eye of the horseshoe crab (Kikuchi et al., 1962), the sympathetic ganglion cells of the Northern leopard frog (Blackman et al., 1963), and the flexo-tibialis and flight muscles of several lepidopteran species (Huddart, 1966).

Based on our simulations, we hypothesize that such reductions in spike amplitude with increased $[K^+]_o$ or E_K are caused by two mechanisms. First, the increased $V_{\rm rest}$ directly reduces the potential difference between spike onset and peak depolarization. Second, at high E_K , K^+ conductance remains elevated throughout the oscillation period, and thus exerts a significant negative effect on the build-up of depolarization during an action potential.



4.6 Perspectives

While our present analysis provides a plausible explanation of how EOD frequency differences between males and females arise from modulation of the K^+ buffering capacity of the astrocytic syncytium, it will be important for future studies to consider other factors that might contribute to the development and maintenance of this sexual dimorphism, as well as to investigate how the proposed mechanism might generalize beyond the current study system.

For example, in our model we assume that areal densities on astrocytes of the Na $^+$ /K $^+$ -ATPase or K $^+$ channels implicated in the uptake of extracellular K $^+$, such as the inwardly rectifying channel K $_{\rm ir}$ 4.1 ((Chever et al., 2010) however, see (D'Ambrosio et al., 2002) for conflicting findings), remain constant. Yet, both experimental and modeling studies have shown that the densities of ion channels on neurons may vary during activity, and that even modest changes in these densities can have pronounced effects on the firing pattern of neurons (Århem et al., 2006; Goldman et al., 2001; Stemmler & Koch, 1999; Zeberg et al., 2015).

Similarly, our model ignores possible variations in interstitial space volume, which affect diffusion parameters and thus, among others, the speed of $[K^+]_o$ clearance and local signaling (Syková & Nicholson, 2008). However, even under physiological conditions, the changes in this volume can be dramatic — for example, transitioning from the awake state to natural sleep is associated with a 60% increase in the interstitial space of the whole brain in mice (Xie et al., 2013).

Finally, the question arises whether the proposed $E_{\rm K}$ -based frequency regulation mechanism is specific to sustained spontaneous oscillations in the Pn of A. leptorhynchus, or more broadly applicable to other central pattern generators. Fishes of the taxonomic family Apteronotidae provide an excellent opportunity to address this question. In the closely related species A. albifrons, the sexual dimorphism in $f_{\rm EOD}$ is reversed compared to A. leptorhynchus, i.e., females discharge at higher frequencies than males (Dunlap et al., 1998; Kolodziejski et al., 2005). Unfortunately, no information is available currently about the structural organization of astrocytes in relation to pacemaker and relay cells in the Pn of A. albifrons. However, future comparative studies may shed light on this fascinating aspect.

Acknowledgements We would like to thank Masashi Kawasaki (University of Virginia, Charlottesville) for fruitful discussion, as well as the two anonymous reviewers for their helpful comments on the manuscript. This research was supported by Grant 1946910 and Research Experiences for Undergraduates Supplement to Grant 1538505, both from the National Science Foundation (GKHZ); an Advanced Research/Creative Endeavor Award, a PEAK Experiences Trailblazer Award, and a Dr. Andrew I. Schafer Researcher Co-op Scholarship, all from Northeastern University (DH); and a Hungarian State Eötvös Scholarship from the Tempus Public Foundation (DL). We would also

like to acknowledge the generous computational and technical support provided by the Northeastern University Discovery Cluster and ITS Research Computing Department.

Declarations

Conflict of interest The authors declare that they have no conflict of interest.

References

- Århem, P., Klement, G., & Blomberg, C. (2006). Channel density regulation of firing patterns in a cortical neuron model. *Biophysical Journal*, *90*, 4392–4404.
- Bachrathy, D., & Stépán, G. (2012). Bisection method in higher dimensions and the efficiency number. *Periodica Polytechnica Mechanical Engineering*, 56, 81–86.
- Bastian, M., Heymann, S., Jacomy, M. (2009). Gephi: an open source software for exploring and manipulating networks. *Third International AAAI Conference on Weblogs and Social Media*.
- Baylor, D. A., & Nicholls, J. G. (1969). Changes in extracellular potassium concentration produced by neuronal activity in the central nervous system of the leech. *Journal of Physiology*, 203, 555–569.
- Bellot-Saez, A., Cohen, G., van Schaik, A., Ooi, L., Morley, J. W., & Buskila, Y. (2018). Astrocytic modulation of cortical oscillations. *Scientific Reports*, 8, 11565.
- Bellot-Saez, A., Kékesi, O., Morley, J. W., & Buskila, Y. (2017). Astrocytic modulation of neuronal excitability through K⁺ spatial buffering. *Neuroscience and Biobehavioral Reviews*, 77, 87–97.
- Bennett, M. V. L. (1971). Electric organs. In Fish Physiology, Vol. 5: Sensory Systems and Electric Organs (eds. W. S. Hoar and D. J. Randall), pp. 347–491. New York: Academic Press.
- Blackman, J. G., Ginsborg, B. L., & Ray, C. (1963). Some effects of changes in ionic concentration on the action potential of sympathetic ganglion cells in the frog. *Journal of Physiology*, 167, 374–388.
- Brocard, F., Shevtsova, N. A., Bouhadfane, M., Tazerart, S., Heinemann, U., Rybak, I. A., & Vinay, L. (2013). Activity-dependent changes in extracellular Ca²⁺ and K⁺ reveal pacemakers in the spinal locomotor-related network. *Neuron*, 77, 1047–1054.
- Canepari, M., Bove, M., Maeda, E., Cappello, M., & Kawana, A. (1997). Experimental analysis of neuronal dynamics in cultured cortical networks and transitions between different patterns of activity. *Biological Cybernetics*, 77, 153–162.
- Chever, O., Djukic, B., McCarthy, K. D., & Amzica, F. (2010). Implication of Kir4.1 channel in excess potassium clearance: an *in vivo* study on anesthetized glial-conditional Kir4.1 knock-out mice. *Journal of Neuroscience*, *30*, 15769–15777.
- D'Ambrosio, R., Gordon, D. S., & Winn, H. R. (2002). Differential role of KIR channel and Na⁺/K⁺-pump in the regulation of extracellular K⁺ in rat hippocampus. *Journal of Neurophysiology*, 87, 87–102.
- de Oliveira-Castro, G. (1955). Differentiated nervous fibers that constitute the electric organ of *Sternarchus albifrons*, Linn. *Anais da Academia Brasileira de Ciências*, 27, 557–564.
- Deng, Q., Rashid, A. J., Fernandez, F. R., Turner, R. W., Maler, L., & Dunn, R. J. (2005). A C-terminal domain directs Kv3.3 channels to dendrites. *Journal of Neuroscience*, 25, 11531–11541.
- Dhooge, A., Govaerts, W., & Kuznetsov, Y. A. (2003). MATCOUNT: a Matlab package for numerical bifurcation analysis of ODEs. *Transactions of Mathematical Software*, 29, 141–164.
- Dunlap, K. D., Thomas, P., & Zakon, H. H. (1998). Diversity of sexual dimorphism in electrocommunication signals and its

- androgen regulation in a genus of electric fish, *Apteronotus*. *Journal of Comparative Physiology A, 183, 77–86.*
- Dye, J. (1991). Ionic and synaptic mechanisms underlying a brainstem oscillator: an *in vitro* study of the pacemaker nucleus of *Apteronotus*. *Journal of Comparative Physiology A*, 168, 521–532.
- Dye, J., & Heiligenberg, W. (1987). Intracellular recording in the medullary pacemaker nucleus of the weakly electric fish, *Apteronotus*, during modulatory behaviors. *Journal of Comparative Physiology A*, 161, 187–200.
- Dye, J. C., & Meyer, J. H. (1986). Central control of the electric organ discharge in weakly electric fish. In T. H. Bullock & W. Heiligenberg (Eds.), *Electroreception*. (pp. 71–102). John Wiley.
- Elekes, K., & Szabo, T. (1985). Synaptology of the medullary command (pacemaker) nucleus of the weakly electric fish (*Apteronotus leptorhynchus*) with particular reference to comparative aspects. *Experimental Brain Research*, 60, 509–520.
- Engler, G., & Zupanc, G. K. H. (2001). Differential production of chirping behavior evoked by electrical stimulation of the weakly electric fish, Apteronotus leptorhynchus. Journal of Comparative Physiology A, 187, 747–756.
- Frankenhaeuser, B., & Hodgkin, A. L. (1956). The after-effects of impulses in the giant nerve fibres of Loligo. *Journal of Physiology*, *131*, 341–376.
- Fröhlich, F., Bazhenov, M., Timofeev, I., Steriade, M., & Sejnowski, T. J. (2006). Slow state transitions of sustained neural oscillations by activity-dependent modulation of intrinsic excitability. *Journal of Neuroscience*, 26, 6153–6162.
- Giaume, C., Kado, R. T., & Korn, H. (1987). Voltage-clamp analysis of a crayfish rectifying synapse. *Journal of Physiology*, 386, 91–112.
- Golbs, A., Nimmervoll, B., Sun, J.-J., Sava, I. E., & Luhmann, H. J. (2011). Control of programmed cell death by distinct electrical activity patterns. *Cerebral Cortex*, 21, 1192–1202
- Goldman, M. S., Golowasch, J., Marder, E., & Abbott, L. F. (2001). Global structure, robustness, and modulation of neuronal models. *Journal of Neuroscience*, 21, 5229–5238.
- Gutierrez, G. J., & Marder, E. (2013). Rectifying electrical synapses can affect the influence of synaptic modulation on output pattern robustness. *Journal of Neuroscience*, 33, 13238–13248.
- Hilgetag, C. C., & Barbas, H. (2009). Are there ten times more glia than neurons in the brain? *Brain Structure and Function*, 213, 365–366.
- Hines, M. L., & Carnevale, N. T. (1997). The NEURON simulation environment. *Neural Computation*, 9, 1179–1209.
- Hines, M. L., & Carnevale, N. T. (2000). Expanding NEURON's repertoire of mechanisms with NMODL. *Neural Computation*, 12, 995–1007.
- Hines, M. L., Davison, A. P., & Muller, E. (2009). NEURON and Python. Frontiers in Neuroinformatics, 3, 1.
- Hodgkin, A. L., & Huxley, A. F. (1952). A quantitative description of membrane current and its application to conduction and excitation in nerve. *Journal of Physiology*, 117, 500–544.
- Huddart, H. (1966). The effect of potassium ions on resting and action potentials in lepidopteran muscle. *Comparative Biochemistry and Physiology*, 18, 131–140.
- Juranek, J., & Metzner, W. (1998). Segregation of behavior-specific synaptic inputs to a vertebrate neuronal oscillator. *Journal of Neu*roscience, 18, 9010–9019.
- Kelley, D. B. (1988). Sexually dimorphic behaviors. Annual Review of Neuroscience, 11, 225–251.
- Kikuchi, R., Naito, K., & Tanaka, I. (1962). Effect of sodium and potassium ions on the electrical activity of single cells in the lateral eye of the horseshoe crab. *Journal of Physiology*, 161, 319–343.
- Kirschbaum, F. (1983). Myogenic electric organ precedes the neurogenic organ in apteronotid fish. *Experientia*, 70, 205–207.



- Kiyoshi, C. M., & Zhou, M. (2019). Astrocyte syncytium: a functional reticular system in the brain. *Neural Regeneration Research*, 14, 595–596.
- Kolodziejski, J. A., Nelson, B. S., & Smith, G. T. (2005). Sex and species differences in neuromodulatory input to a premotor nucleus: a comparative study of substance P and communication behavior in weakly electric fish. *Journal of Neurobiology*, 62, 299–315.
- Lai, H. C., & Jan, L. Y. (2006). The distribution and targeting of neuronal voltage-gated ion channels. *Nature Reviews Neuroscience*, 7, 548–562.
- Lodish, H., Berk, A., Zipursky, S. L., Matsudaira, P., Baltimore, D., & Darnell, J. (2000). *Molecular Cell Biology*. (4th ed.). W.H.
- Lucas, K. M., Warrington, J., Lewis, T. J., & Lewis, J. E. (2019). Neuronal dynamics underlying communication signals in a weakly electric fish: implications for connectivity in a pacemaker network. *Neuroscience*, 401, 21–34.
- Lux, H. D., Heinemann, U., & Dietzel, I. (1986). Ionic changes and alterations in the size of the extracellular space during epileptic activity. Advances in Neurology, 44, 619–639.
- Lux, H. D., & Neher, E. (1973). The equilibration time course of [K⁺]_o in cat cortex. *Experimental Brain Research*, 17, 190–205.
- Ma, B., Buckalew, R., Du, Y., Kiyoshi, C. M., Alford, C. C., Wang, W., McTigue, D. M., Enyeart, J. J., Terman, D., & Zhou, M. (2016). Gap junction coupling confers isopotentiality on astrocyte syncytium. *Glia*, 64, 214–226.
- Meyer, J. H., Leong, M., & Keller, C. H. (1987). Hormone-induced and maturational changes in electric organ discharges and electroreceptor tuning in the weakly electric fish *Apteronotus*. *Journal of Comparative Physiology A*, 160, 385–394.
- Moody, W. J., Futamachi, K. J., & Prince, D. A. (1974). Extracellular potassium activity during epileptogenesis. *Experimental Neurology*, 42, 248–263.
- Moortgat, K. T., Bullock, T. H., & Sejnowski, T. J. (2000a). Precision of the pacemaker nucleus in a weakly electric fish: network versus cellular influences. *Journal of Neurophysiology*, 83, 971–983.
- Moortgat, K. T., Bullock, T. H., & Sejnowski, T. J. (2000b). Gap junction effects on precision and frequency of a model pacemaker network. *Journal of Neurophysiology*, 83, 984–997.
- Nilsson, G. E., Pérez-Pinzón, M., Dimberg, K., & Winberg, S. (1993).
 Brain sensitivity to anoxia in fish as reflected by changes in extracellular K⁺ activity. American Journal of Physiology, 264, R250–R253.
- Petracca, M., Vancea, R. O., Fleysher, L., Jonkman, L. E., Oesingmann, N., & Inglese, M. (2016). Brain intra- and extracellular sodium concentration in multiple sclerosis: a 7 T MRI study. *Brain*, 139, 795–806.
- Prince, D. A., Lux, H. D., & Neher, E. (1973). Measurement of extracellular potassium activity in cat cortex. *Brain Research*, 50, 489–495.
- Rasmussen, R., Nicholas, E., Petersen, N. C., Dietz, A. G., Xu, Q., Sun, Q., & Nedergaard, M. (2019). Cortex-wide changes in extracellular potassium ions parallel brain state transitions in awake behaving mice. *Cell Reports*, 28, 1182–1194.
- Rasmussen, R., O'Donnell, J., Ding, F., & Nedergaard, M. (2020). Interstitial ions: a key regulator of state-dependent neural activity? *Progress in Neurobiology*, 193, 101802.
- Rice, M. E., & Nicholson, C. (1988). Behavior of extracellular K⁺ and pH in skate (*Raja erinacea*) cerebellum. *Brain Research*, 461, 328–334.
- Ridley, B., Nagel, A. M., Bydder, M., Maarouf, A., Stellmann, J.-P., Gherib, S., et al. (2018). Distribution of brain sodium long and short relaxation times and concentrations: a multi-echo ultra-high field ²³Na MRI study. *Scientific Reports*, 8, 4357.
- Schaefer, J. E., & Zakon, H. H. (1996). Opposing actions of androgen and estrogen on in vitro firing frequency of neuronal oscillators in the electromotor system. *Journal of Neuroscience*, 16, 2860–2868.

- Shifman, A. R., Sun, Y., Benoit, C. M., & Lewis, J. E. (2020). Dynamics of a neuronal pacemaker in the weakly electric fish Apteronotus. Scientific Reports, 10, 16707.
- Sîrbulescu, R. F., Ilieş, I., Meyer, A., & Zupanc, G. K. H. (2017). Additive neurogenesis supported by multiple stem cell populations mediates adult spinal cord development: a spatiotemporal statistical mapping analysis in a teleost model of indeterminate growth. *Developmental Neurobiology*, 77, 1269–1307.
- Sîrbulescu, R. F., Ilieş, I., & Zupanc, G. K. H. (2014). Quantitative analysis reveals dominance of gliogenesis over neurogenesis in an adult brainstem oscillator. *Developmental Neurobiology*, 74, 934–952.
- Smith, G. T., Lu, Y., & Zakon, H. H. (2000). Parvocells: a novel interneuron type in the pacemaker nucleus of a weakly electric fish. *Journal of Comparative Neurology*, 423, 427–439.
- Somjen, G. G. (2004). *Ions in the Brain: Normal Function, Seizures, and Stroke*. Oxford University Press.
- Spong, K. E., & Robertson, R. M. (2013). Pharmacological blockade of gap junctions induces repetitive surging of extracellular potassium within the locust CNS. *Journal of Insect Physiology*, 59, 1031–1040.
- Spray, D. C., Harris, A. L., & Bennett, M. V. L. (1981). Equilibrium properties of a voltage-dependent junctional conductance. *Journal* of *General Physiology*, 77, 77–93.
- Stemmler, M., & Koch, C. (1999). How voltage-dependent conductances can adapt to maximize the information encoded by neuronal firing rate. *Nature Neuroscience*, 2, 521–527.
- Syková, E., & Nicholson, C. (2008). Diffusion in brain extracellular space. *Physiological Reviews*, 88, 1277–1340.
- Syková, E., Rothenberg, S., & Krekule, I. (1974). Changes of extracellular potassium concentration during spontaneous activity in the mesencephalic reticular formation of the rat. *Brain Research*, 79, 333–337.
- Thulborn, K. R., Davis, D., Adams, H., Gindin, T., & Zhou, J. (1999). Quantitative tissue sodium concentration mapping of the growth of focal cerebral tumors with sodium magnetic resonance imaging. *Magnetic Resonance in Medicine*, 41, 351–359.
- Tong, X., Ao, Y., Faas, G. C., Nwaobi, S. E., Xu, J., Haustein, M. D., et al. (2014). Astrocyte Kir4.1 ion channel deficits contribute to neuronal dysfunction in Huntington's disease model mice. *Nature Neuroscience*, 17, 694–703.
- Trimmer, J. S., & Rhodes, K. J. (2004). Localization of voltage-gated ion channels in mammalian brain. *Annual Review of Physiology*, 66, 477–519.
- Turner, R. W., & Moroz, L. L. (1995). Localization of nicotinamide adenine dinucleotide phosphate-diaphorase activity in electrosensory and electromotor systems of a gymnotiform teleost, Apteronotus leptorhynchus. Journal of Comparative Neurology, 356, 261–274.
- Verkhratsky, A., & Nedergaard, M. (2018). Physiology of astroglia. Physiological Reviews, 98, 239–389.
- von Bartheld, C. S., Bahney, J., & Herculano-Houzel, S. (2016). The search for true numbers of neurons and glial cells in the human brain: a review of 150 years of cell counting. *Journal of Comparative Neurology*, 524, 3865–3895.
- Walz, W. (2000). Role of astrocytes in the clearance of excess extracellular potassium. *Neurochemistry International*, 36, 291–300.
- Wang, F., Smith, N. A., Xu, Q., Fujita, T., Baba, A., Matsuda, T., Takano, T., Bekar, L., Nedergaard, M. (2012). Astrocytes modulate neural network activity by Ca²⁺-dependent uptake of extracellular K⁺. Science Signaling, 5, ra26.
- Waxman, S. G., Pappas, G. D., & Bennett, M. V. L. (1972). Morphological correlates of functional differentiation of nodes of Ranvier along single fibers in the neurogenic electric organ of the knife fish Sternarchus. Journal of Cell Biology, 53, 210–224.



- Xie, L., Kang, H., Xu, Q., Chen, M. J., Liao, Y., Thiyagarajan, M., et al. (2013). Sleep drives metabolite clearance from the adult brain. *Science*, 342, 373–377.
- Yamamoto, T., Maler, L., Hertzberg, E. L., & Nagy, J. I. (1989). Gap junction protein in weakly electric fish (Gymnotide [sic]): immunohistochemical localization with emphasis on structures of the electrosensory system. *Journal of Comparative Neurology*, 289, 509–536.
- Zeberg, H., Robinson, H. P., & Århem, P. (2015). Density of voltage-gated potassium channels is a bifurcation parameter in pyramidal neurons. *Journal of Neurophysiology*, 113, 537–549.
- Zupanc, G. K. H. (2017). Dynamic neuron-glia interactions in an oscillatory network controlling behavioral plasticity in the weakly electric fish. Apteronotus leptorhynchus. Frontiers in Physiology, 8, 1087.
- Zupanc, G. K. H. (2020). Development of a sexual dimorphism in a central pattern generator driving a rhythmic behavior: the role of glia-mediated potassium buffering in the pacemaker nucleus of the weakly electric fish Apteronotus leptorhynchus. Developmental Neurobiology, 80, 6–15.

- Zupanc, G. K. H., Amaro, S. M., Lehotzky, D., Zupanc, F. B., & Leung, N. Y. (2019). Glia-mediated modulation of extracellular potassium concentration determines the sexually dimorphic output frequency of a model brainstem oscillator. *Journal of Theoretical Biology*, 471, 117–124.
- Zupanc, G. K. H., Banks, J. R., Engler, G., & Beason, R. C. (2003).
 Temperature dependence of the electric organ discharge in weakly electric fish. In B. J. Ploger & K. Yasukawa (Eds.), Exploring Animal Behavior in Laboratory and Field: An Hypothesis-testing Approach to the Development, Causation, Function, and Evolution of Animal Behavior. (pp. 85–94). Academic Press.
- Zupanc, G. K. H., Ilieş, I., Sîrbulescu, R. F., & Zupanc, M. M. (2014). Large-scale identification of proteins involved in the development of a sexually dimorphic behavior. *Journal of Neurophysiology*, 111, 1646–1654.

Publisher's Note Springer Nature remains neutral with regard to jurisdictional claims in published maps and institutional affiliations.

